Effects of secondary ice processes on a stratocumulus to cumulus transition during a cold-air outbreak

Michail Karalis [a], Georgia Sotiropoulou [b,c,d,*], Steven J. Abel [e], Elissavet Bossioli [a],
Paraskevi Georgakaki [d], Georgia Methymaki [a], Athanasios Nenes [b,d], Maria Tombrou [a]

[a] Division of Environmental Physics and Meteorology, Department of Physics, University of Athens, Athens, Greece
[b] Institute of Chemical Engineering Sciences, Foundation for Research and Technology Hellas, Patras, Greece
[c] Department of Meteorology, Stockholm University, Stockholm, Sweden
[d] Laboratory of Atmospheric Processes and their Impacts, ENAC, Ecole Polytechnique Fédérale de Lausanne, Lausanne, Switzerland
[e] Met Office, Exeter, United Kingdom

ARTICLE INFO

ABSTRACT

The representation of boundary layer clouds during marine Cold-Air Outbreaks (CAO) remains a great challenge for weather prediction models. Recent studies have shown that the representation of the transition from closed stratocumulus clouds to convective cumulus open cells largely depends on microphysical and precipitation processes, which secondary ice production (SIP) may strongly modulate. In this study we use the Weather Research and Forecasting model to investigate the impact of the most well-known SIP mechanisms (Hallett-Mossop, mechanical break-up upon collisions between ice particles and drop-shattering) on a CAO case observed north of the United Kingdom in 2013. While Hallett-Mossop is the only SIP process extensively implemented in atmospheric models, our results indicate that the other two SIP mechanisms are also favored in the examined conditions. Activation of drop-shattering and especially collisional break-up can result in enhanced riming, ice depositional growth and/or ice aggregation. The first two processes quicken liquid depletion in the stratocumulus cloud, while along with aggregation, they enhance precipitation. The increased precipitation results in enhanced evaporation/sublimation in the sub-cloud layer, promoting boundary-layer decoupling, which further accelerates the onset of the stratocumulus break-up. However, the strong sensitivity to the expression of terminal velocity of the precipitating particles and the rimed fraction of cloud ice/snow suggests that the robust implementation of SIP to improve CAO predictions requires data from a large number of CAO events.

1. Introduction

Cold Air Outbreaks (CAOs) (Walsh et al., 2001) are meridional advection events of cold air generated in the polar cap over the warmer mid-latitude continental or marine surfaces and are more frequently observed in the Northern Hemisphere during winter (Fletcher et al., 2016). CAOs are significant components of mid-latitude weather systems, often being associated with severe weather events with harmful impacts on vegetation, building infrastructure and even human life (Rogers and Rohli, 1991; Smith and Sheridan, 2018). During the equatorward migration of the air masses associated with CAOs, sensible and latent heat fluxes gradually increase eventually leading to the formation of clouds. The intricate boundary layer changes that take place along the air mass trajectory translate into changes in the cloud morphology,

which usually result in a stratocumulus-to-cumulus transition (SCT) (Xiao et al., 2012; Chung et al., 2012; Sandu and Stevens, 2011).

Bretherton and Wyant (1997) argued that the SCT is driven by the increased surface latent flux in the subtropics, where sensible fluxes are generally weaker. According to their theory, increased sea surface temperatures (SSTs) at the lower latitudes lead to deepening of the planetary boundary layer (PBL) and increased moisture flux from the surface to the cloud layer, which further enhances buoyancy and latent heat release. Buoyancy fluxes then increase faster in the cloud compared to the sub-cloud layer, which eventually results in cloud-surface decoupling and break-up of the stratocumulus layer. That SST rise is the sole driver of the SCT was however disputed by Abel et al. (2017) and Yamaguchi et al. (2017). Both studies concluded that the decoupling of the boundary layer, responsible for the initiation of the transition, is

driven by the evaporation of precipitation, which locally cools the air, forming a temperature inversion in the sub-cloud layer that suppresses the upward vapor transport. Microphysical processes that affect precipitation may therefore have a strong effect on SCT. In this regard, secondary ice production (SIP) may influence SCT. Indeed, Abel et al. (2017) postulated that SIP strongly promoted the development of precipitation during a CAO event observed close to the United Kingdom (UK). SIP initiation was indicated by a substantial increase in ice crystal number concentration (ICNC) in the cumulus region compared to the stratiform regime, which could not be attributed to changes in primary ice nucleating particle (INP) concentrations. Studies of convective systems have shown that SIP can affect the precipitation intensity and onset of cloud glaciation (e.g. Taylor et al., 2016; Sullivan et al., 2018; Zipori et al., 2018), but the importance of all possible SIP mechanisms remains poorly understood.

The most well-known SIP mechanism is the production of ice splinters after a drop rimes onto an ice particle at temperatures between −8 °C to −3 °C (Hallett and Mossop, 1974). This process is known as Hallett-Mossop and is the only SIP mechanism that has been widely implemented in weather prediction and climate models. However, observational evidence of SIP has been found outside the Hallett-Mossop optimal temperature range (Heymsfield and Willis, 2014; Ladino et al., 2017; Mignani et al., 2019; Korolev et al., 2020). Several SIP mechanisms in addition to Hallett-Mossop have been identified and studied in laboratory experiments (Field et al., 2017; Korolev and Leisner, 2020). However, two main mechanisms have been observed in real atmospheric conditions: drop-shattering (Heymsfield and Willis, 2014; Korolev et al., 2020; Luke et al., 2021) and fragmentation due to break-up upon collision of ice particles (Rangno and Hobbs, 2001; Schwarzenboeck et al., 2009). A number of recent modeling studies have highlighted the importance of these two SIP mechanisms in convective (Phillips et al., 2017b; Qu et al., 2020; Sullivan et al., 2018), polar stratocumulus (Sotiropoulou et al., 2020, 2021a; Zhao et al., 2021) and orographic cloud conditions (Dedekind et al., 2021; Lauber et al., 2021; Georgakaki et al., 2021). Moreover, modeling studies have shown that the combination of multiple SIP mechanisms is required to explain the observed ICNCs in convective and stratocumulus clouds (Qu et al., 2020; Sotiropoulou et al., 2020; Zhao et al., 2021). Yet, no study so far has investigated their potential role during a SCT.

In this study we use the Weather Research and Forecasting (WRF) mesoscale numerical model (Skamarock et al., 2008) to investigate the impact of the most well-known SIP mechanisms (Hallett-Mossop, droplet shattering and collisional break-up) on a SCT observed during a CAO event that occurred north of UK in 2013 (Abel et al., 2017; Lloyd et al., 2018). The version of WRF used in this study includes updated microphysics to treat all main SIP mechanisms (Sotiropoulou et al., 2021a; Georgakaki et al., 2021) in the Morrison et al. (2005) cloud microphysics scheme.

2. Observations

This study focuses on the CAO event that took place north of UK on 24 November 2013. The southward advection of the cold air mass is indicated by a strong northerly flow (Fig. 1a) that spans the sea from latitudes higher than 80°N to the shore of Germany, travelling through the Scandinavian Peninsula and the UK. There is a prominent SST gradient along the wind direction with temperatures rising downstream, while a SCT was observed (Abel et al., 2017) near the Norwegian coastline (Fig. 1b). The transition was investigated with the use of the Facility of Airborne Atmospheric Measurements (FAAM) BAe-146 research aircraft which conducted in situ measurements of atmospheric parameters and microphysical cloud properties (Abel et al., 2017). The flight lasted almost 6 h and covered a 5° × 5° area surrounding the location of the transition. Aircraft observations included in-cloud measurements as well as several vertical profiles, in both the stratocumulus and the cumulus area, extending from near the sea-surface to altitudes above the boundary layer.

2.1. Instrumentation

The BAe-146 research aircraft was equipped with various instruments and probes to conduct thermodynamic and microphysical measurements across the SCT, a description of which can be found in Abel et al. (2017). For the needs of the present study, observations of liquid water content (LWC) and LWP are utilized, which were collected with a Nevzorov probe (Korolev et al., 1998) and a MARSS radiometer (McGrath and Hewison, 2001), respectively. The total water probe (Nicholls et al., 1990) measured the total water (vapor + liquid + ice) mixing ratio q_T. Number concentrations of particles within the [100 μm–6.4 mm] and [10 μm–1280 mm] size range were measured with a CIP-100 probe (Baumgardner et al., 2011) and a 2DS probe (Lawson et al., 2006), respectively. The two probes were fitted with anti-shatter tips (Korolev et al., 2013), while particle interarrival filtering (Field et al., 2006) was applied to the measurements to mitigate artifacts from ice particle shattering on the probe. Imaginary of highly irregular particles were used to determine ice number concentrations (N_{ice}) from the
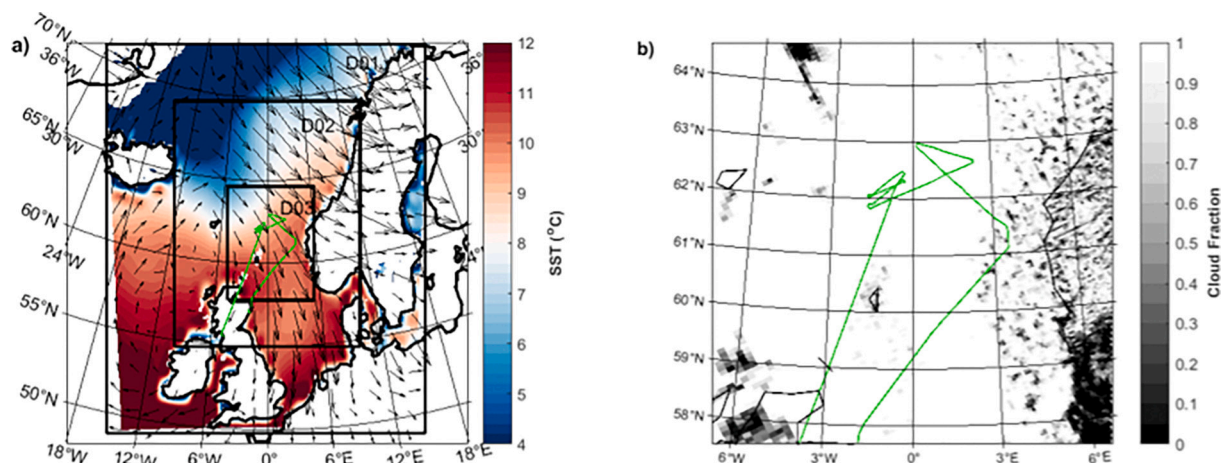

Fig. 1. Maps depicting (a) the surface wind velocity and direction (vectors), sea surface temperature horizontal distribution (colors) and model domain boundaries (black lines) at 12:00 UTC on 24 November 2013 and (b) the Moderate Resolution Imaging Spectroradiometer (MODIS) cloud fraction at 11:55 UTC on 24 November 2013. Aircraft trajectory is indicated in both panels with a green line. Note the different axes between the two panels. (For interpretation of the references to colour in this figure legend, the reader is referred to the web version of this article.)

2DS probe, while Ice Water Content (IWC) was derived using the Brown and Francis (1995) mass-dimension relationship. Finally, air temperature values along the flight trajectory were recorded using a deiced Rosemount/Goodrich type 102 total air temperature sensor and vertical velocities were measured with a turbulence probe.

2.2. Stratiform and cumulus conditions

As the aircraft flew across the SCT, the measurements showed a PBL deepening from 1.85 km to 2.14 km and a steep decline in liquid water path (LWP), cloud droplet and accumulation mode aerosol number concentrations (Abel et al., 2017). This reduction is attributed to aerosol scavenging due to enhanced collision-coalescence processes and subsequent precipitation across the transition. Such steep changes in aerosol and cloud particle concentrations have been observed during other stratocumulus-to-cumulus transitions (Terai et al., 2014; Lloyd et al., 2018), with cloud droplet concentrations as low as 20–40 cm^{-3} in the cumulus regime (Terai et al., 2014).

The stratiform cloud layer, observed at temperatures between −13.9 °C and −8.2 °C (Fig. 2a, b), consisted mostly of super-cooled liquid water with a mean droplet diameter round 22 µm at cloud top and low concentrations of ice (see figure 4a and 5 in Abel et al., 2017). This was inferred by a combined size distribution from the CDP, 2DS, and CIP-100 data (figure 5 in Abel et al., 2017,) which revealed a distinct mode in the stratiform regime at particle sizes (diameters) between 10 and 25 µm, which represent the liquid cloud drops, and a tail of the distribution at larger sizes that represent ice and precipitation-sized particles. Furthermore, particle imaginary revealed the presence of dendrites and graupels within and below the cloud layer, while precipitation was composed of both ice particles and drizzle. The maximum in-cloud vertical velocity (w_{max}) recorded within the stratocumulus clouds is 0.87 m s^{-1}.

The cumulus cloud bases were significantly lower, falling within the Hallett-Mossop temperature range (Fig. 2e, f), while the presence of ice hydrometeors and precipitation sized particles was much more prevalent. This is suggested by the particle size distribution of the sampled cumulus clouds, which is bimodal with a second peak at sizes between

200 and 300 µm (figure 5 in Abel et al., 2017). LWC was significant lower in this cloud region (Fig. 2d), while cloud probe imaginary revealed a substantial increase in ice number, mainly in the form of rimed particles and columnar ice (see figure 4b in Abel et al., 2017). The measured in-cloud w_{max} within the cumulus regime is 1.82 m s^{-1}, about two times larger than the value found in the stratocumulus clouds. However, these measurements are not necessarily represenative of the turbulence conditions within this region, as the aircraft collected a limited number of samples (about four times less than those collected within the stratiform clouds).

3. Model

3.1. Model set-up

Simulations are performed using the 4.0.1 version of the WRF model. The area of study is divided in three domains two-way nested within each other (Fig. 1), with horizontal grid resolution ranging from 9 km in the parent domain (D01) to 3 km in D02 and 1 km in D03, in which the SCT takes place. The respective time-steps in each domain are 54 s, 18 s and 6 s. D01 is centered at 62.25°N, 0°E and covers an area of 2088 km (west-east) and 2781 km (north-south), while D03 covers an area of 592 km and 778 km in the zonal and meridional direction, respectively. Vertical resolution in all domains consists of a total of 70 vertical levels from the surface to the model top, set at the 10 hPa isobar, while the first level corresponds to an altitude of 15 m. The lower 29 levels are located below 3 km, following the set-up of the Unified Model simulations in Abel et al. (2017). The simulation period is 48 h, starting at 00:00 on 23 November 2013, with the first 24 h considered as spin-up period. The ERA5 reanalysis dataset (Hersbach et al., 2020) is used to initialize the model and set the boundary conditions.

The non-local, 1st order closure YSU (Yonsei University) (Hong et al., 2006) parameterization scheme is selected for the representation of PBL physics in our simulations; YSU was found to conform better with observations compared to the local 3rd order closure MYNN3 (Mellor-Yamada-Nakanishi-Niino) (Nakanishi and Niino, 2006) scheme (not shown). The RRTMG scheme (Iacono et al., 2008) is applied for both
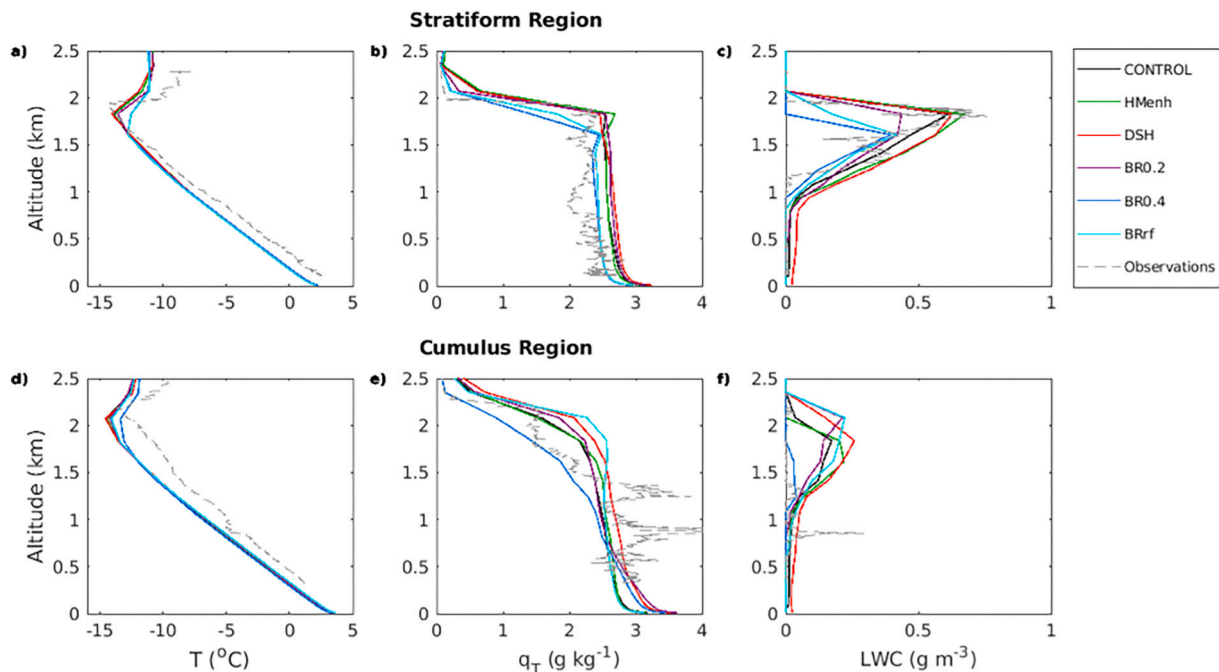

Fig. 2. Vertical profiles of (a,d) temperature (T), (b,e) total water mixing ratio (q_T) and (c,f) liquid water content (LWC), derived from the observed stratocumulus and cumulus regimes at 1100 UTC. All model data are averaged over a 10×10 km^2 area that surrounds the location of the profiling measurements (dashed grey lines), except q_T which shows the maximum model values. Only LWC values >0.01 g m^{-2} are included in the averaging.

shortwave and longwave radiation. The Grell 3D cumulus parameterization scheme is used only in D01, where the horizontal resolution is too coarse to enable the explicit representation of convective updrafts. However, by performing a no-cumulus-scheme sensitivity test and a test with the Kain-Fritsch (KF) scheme (Kain and Fritsch, 1993) in D01, we were able to assess that the choice of the convection parameterization scheme has hardly any impact on the simulated SCT (not shown).

For the cloud microphysical processes, the Morrison 2-moment bulk scheme (Morrison et al., 2005) is applied, which account for 5 hydrometeor types (cloud droplet, rain, cloud ice, snow and graupel). The mass concentration is predicted for all hydrometeors, while number concentration is only predicted for rain, cloud ice, snow and graupel. Due to the model not being coupled with chemistry, a fixed value of 200 cm^{-3} is assigned to cloud droplet number concentration (N_{drop}) in the default WRF version. Here, the default N_{drop} is replaced by the value of 118 cm^{-3} in the stratocumulus region (approximately at longitudes $\leq 2.5°E$, see Fig. 3a) and 19 cm^{-3} in the cumulus region (longitudes $>2.5°E$), in agreement with the mean aircraft observations. A sensitivity test with a constant N_{drop} of 118 cm^{-3} across the domain could not reproduce a defined SCT transition (Fig. S1). These results are in line with the study of Yamaguchi et al. (2017), who showed that a spatially uniform N_{drop} suppresses precipitation with significant implications for the SCT initiation (Yamaguchi et al., 2017).

3.2. SIP parameterizations

The standard Morrison scheme (Morrison et al., 2005) accountd only for one SIP mechanism, the Hallet-Mossop process. The description of this mechanism follows Reisner et al. (1998), which predicts a maximum production of 350 splinters per milligram of rime generated around $-5°C$. Thus, the efficiency of the process is set to unity at $-5°C$, zero for temperatures below $-8°C$ and above $-3°C$ and adjusts linearly between these two limits. Furthermore, Hallett-Mossop is activated only if two conditions are met: (a) snow (or graupel) mass mixing ratios must be >0.1 g kg^{-1} and (b) cloud liquid (or rain) water mass mixing ratios should be >0.5 (or 0.1) g kg^{-1}.

Sotiropoulou et al. (2021a, 2021b) implemented a parameterization for collisional break-up in Morrison scheme, following the description developed by Phillips et al. (2017a). This process is initiated after cloud ice-snow, cloud ice-graupel, snow-snow, snow-graupel ande graupel-graupel collisions. It is assumed that the collisions that do not contribute to aggregation initiate break-up. Phillips et al. (2017a) is a physically-based parameterization that predicts the number of generated fragments as a function of collisional kinetic energy, while the effect of the colliding particles' size, rimed fraction and ice habit is also accounted. Morrison scheme however does not predict rimed fraction and ice habit, that these parameters have to be prescribed. To account for underestimations in collisional kinetic energy when the terminal velocity of the two colliding particles is similar ($u_1 \approx u_2$), the corrections in the mass- or number-weighted difference in terminal velocity (Δu_{12}) proposed by Mizuno (1990) and Reisner et al. (1998) are adapted. All generated fragments are added to the cloud ice category. When snowflakes collide with each other, it is assumed that 0.1% of the colliding mass is transferred to the generated fragments (Phillips et al., 2017a). A detailed description of the implemented equations can be found in Appendix B of Sotiropoulou et al. (2021a).

Georgakaki et al. (2021) implemeted a description of drop-shattering in the Morrison scheme, following Phillips et al. (2018). This mechanism is initiated after raindrop-INP (immersion freezing), raindrop-snow, raindrop-graupel and raindrop-cloud ice collisions. For ice multiplication due to raindrop-INP and raindrop-cloud ice interactions we utilize the parameterization referred as 'mode 1' in Phillips et al. (2018), which concerns the accretion of small particles by more massive raindrops. For snow-raindrop and graupel-raindrop collisions, the 'mode 2' parameterization is adapted. Mode 1 can generate both tiny and big fragments; the former are added to the cloud ice category, while the latter are considered snow. The new tiny fragments are assumed to have a fixed diameter at 10^{-6} m and a constant ice density of 500 kg m^{-3}, while the rest the colliding rain mass is transfer to snow. Freezing probability (P_{fr}) in this mode is set to unity and zero, at temperatures below $-6°C$ and above $-3°C$, respectively, while it takes intermediate values at temperatures between $-6°C$ and $-3°C$. Similarly, shattering probability (P_{sh})
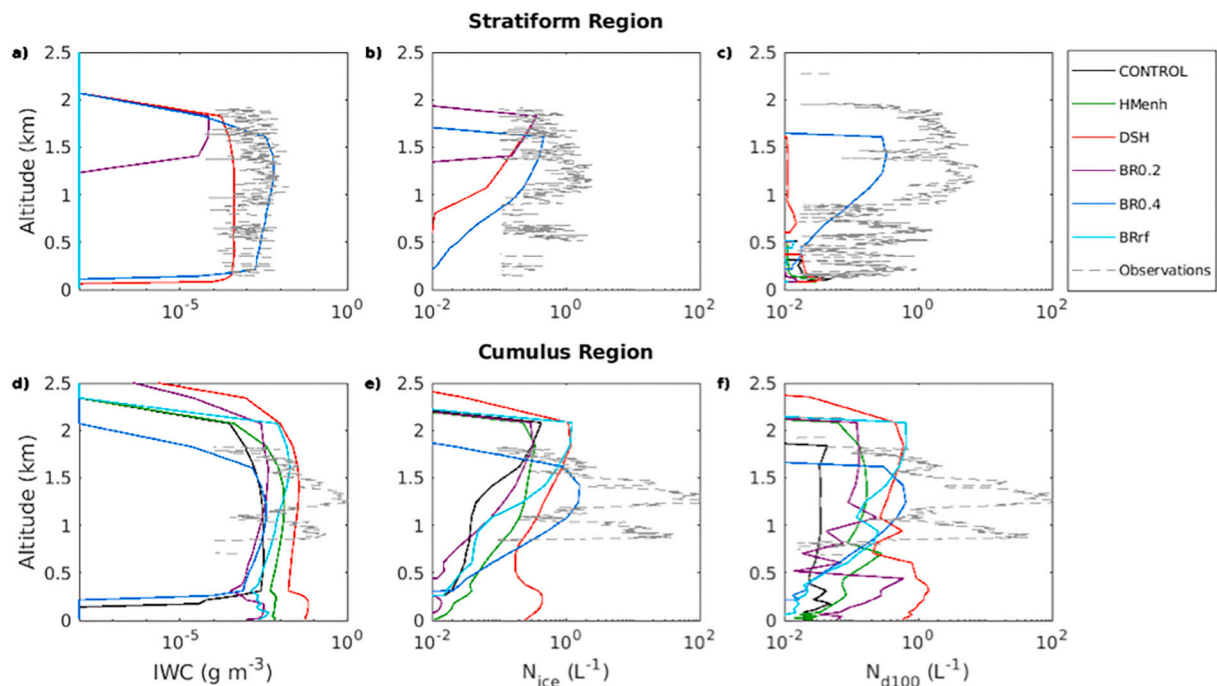

Fig. 3. Same as Fig. 2 but for profiles of (a,d) Ice Water Content (IWC), (b,e) ice number concentration (N_{ice}) and number concentration of particles with sizes (diameters) >100 μm (N_{d100}). Only IWC and particle number values $>10^{-8}$ g m^{-3} and 0.01 L^{-1}, respectively, are included in the averaging. Note the logarithmic horizontal axes.

is a function of raindrop size, set to 0 and 1 at sizes smaller than 50 μm and larger than 60 μm, respectively. Eventually, the probability for this mechanism to occur is given by the product of these two terms $P_{fr}P_{sh}$. The choice of the above temperature and size threshold are based on a pool of laboratory datasets (see table 1 in Phillips et al., 2018). Mode 2 can only generate tiny fragments. The number of generated fragments for mode 2 is a function of collisional kinetic energy, thus the the mass- or number-weighted Δu_{12} corrections (Mizuno, 1990; Reisner et al., 1998) are also applied here. In this mode only 0.1% of the colliding mass is transferred to the generated fragments (Phillips et al., 2018).

3.3. Sensitivity simulations

The CONTROL simulation is conducted using the standard Morrison scheme (Morrison et al., 2005), which accounts only for Hallett-Mossop. However, Atlas et al. (2020) recently showed that removing the ice and liquid mass thresholds (see Section 3.2) from the Hallett-Mossop description improves the microphysical representation of Southern Ocean stratocumulus clouds. Following their suggestions, we perform a sensitivity test with a similar set-up that is expected to enhance the efficiency of this mechanism. This test is referred as HMenh in the text. To assess the efficiency of drop-shattering in the examined conditions, we perform an additional simulation (DSH) with the modified Morrison scheme by Georgakaki et al. (2021).

Finally, to investigate the efficiency of collisional break-up we have to prescribe rimed fraction, as this parameter is not predicted by the Morrison scheme. However, previous studies have shown that the performance of Phillips et al. (2017a) parameterization can be very sensitive to this assumption (Sotiropoulou et al., 2021a, 2021b). For this reason, we perform three sensitivity simulations with active break-up, but different treatment of the rimed fraction for the cloud-ice or snow particle that undergoes break-up. In BR0.2 the rimed fraction of these two ice species remains fixed at 0.2, in BR0.4 a high rimed fraction of 0.4 is assumed, while in BRrf a varying treatment of this parameter is allowed. This is diagnosed as the ratio between the sum of source terms for the mass mixing ratio of the respective frozen hydrometeor, calculated from collisions with liquid particles, over the sum of all mixing ratio source terms. Sink terms are not included in this diagnostic formulation, as they are assumed to affect equally both the rimed and unrimed part of the particle. Since the rimed particles in this bulk scheme are represented by the graupel category, it is reasonable to consider that a maximum rimed fraction of 0.4 (<50%) is representative for cloud ice and snow in BRrf. If the diagnosed value is zero, no break-up occurs. A planar ice habit is assumed in all three simulations, as this category encompasses all ice shapes except dendrites and is more suitable for the examined temperature range (Phillips et al., 2017a).

A summary of all sensitivity tests is presented in Table 1. Simulations with all SIP mechanisms (including the enhanced Hallett-Mossop set-up)

are also conducted, a summary of which is given in Table S1. Only, a short discussion on these simulations is given in the main manuscript, since they do not differentiate substantially from the BR runs (more details can be found in the Supplementary Information).

4. Results

4.1. Vertical structure

Figs. 2 and 3 shows vertical profiles of thermodynamic and microphysical properties, averaged over a 10×10 km^2 area that encompasses the location of the aircraft profile measurements (indicated with blue dots in Fig. 4), both upstream and downstream of the transition (see profiles P6 and P9 in Fig. 2c of Abel et al. (2017)). Exceptions to this are the q_T profiles, which show the maximum value at each atmospheric level, instead of the mean. This way, averaging between precipitation and non-precipitating profiles is avoided, since the aircraft sampled precipitating clouds. CONTROL correctly predicts a well-mixed PBL capped by a temperature inversion at ~1.8 km (Fig. 2a) in the stratocumulus region, which however is about 1 °C colder than the observations in the lowest kilometer of the atmosphere. LWC (cloud and rain water) and q_T profiles (Fig. 2b,c) are in very good agreement with the measurements, but the model does not predict any significant ice content (Fig. 3a–b) or particles with sizes larger than 100 μm (N_{d100}). In contrast, the observations indicate the presence of ice and drizzle (see Section 2.2).

HMenh and DSH produce very similar temperature, LWC and q_T profiles to CONTROL, while activation of collisional break-up decreases LWC, with more significant underestimations in BR0.4 and BRrf simulations (Fig. 2c). This leads to an incorrect lowering of the cloud top in these simulations, which also results in a lowering of the PBL height (Fig. 2a) and the depth of the mixed q_T layer (Fig. 2b). All simulations collectively fail to reproduce ice in the stratocumulus regime (Fig. 3a–b) except BR0.2, DSH and BR0.4, with the later being closer to observations. However, only BR0. 4 can produce significant N_{d100} concentrations with values as high as 0.3 L^{-1} that are closer to the observed values ~1 L^{-1} (Fig. 3c). Most runs show mere spikes below the cloud base, corresponding to falling precipitation (Fig. 3c). This is liquid in most simulations, except for DSH and BR0.4 which produce a mixture of ice and liquid precipitating particles. Since the stratocumulus cloud lies above the Hallett-Mossop optimal temperature zone (simulated at ~0.5–1 km), it is no surprise that any variations in the treatment of this process do not significantly impact number concentrations.

In the cumulus region, the CONTROL simulation shows a notable underestimation of the air temperature (Fig. 2d). The modeled PBL is about ~1 °C colder below cloud base (~0.75 km), while, this difference becomes substantially larger in the cloud layer, displaying a ~2.4 °C difference with observations at 1.8 km. The increase of the temperature bias with increasing height is partly associated with errors in microphysical processes. While observations indicate the break-up of the stratocumulus layer and the presence of a cumulus cloud at lower altitudes, between 0.8 and 1.5 km (Fig. 2f), the CONTROL simulation maintains the higher stratiform cloud. This cloud sustains significant LWC for cloud-top longwave emission (Fig. 2f), which cools the surrounding air (Fig. 2d). The inability of the model to dissipate the upper cloud and reproduce cloud condensate at lower levels also shows up in the q_T profile (Fig. 2g). While IWC has substantially increased in the cumulus region (Fig. 3d), it remains somewhat underestimated compared to observations. The largest ice number concentrations are produced above 2 km (Fig. 3e), with N_{ice} being substantially underestimated in the 1–1.5 km, where maximum ice production is observed in reality. N_{d100} also remain about 2–3 orders of magnitude lower in CONTROL simulation compared to observations (Fig. 3f).

Varying SIP treatment has little impact on temperature (Fig. 2d) and LWC (Fig. 2f), except for BR0.4, which is the only simulation that successfully reproduces cloud break-up and a more realistic cumuliform

Table 1
Description of the sensitivity simulations considered in this study.

| Sensitivity simulations	Activated SIP mechanism
CONTROL	Hallett-Mossop mechanism (Reisner et al., 1998), allowed once ice particle and liquid drop masses exceed certain thresholds
HMenh	Enhanced Hallett-Mossop efficiency due to removal of the hydrometeor mass thresholds (Atlas et al., 2020)
DSH	Drop shattering (Phillips et al., 2018)
BR0.2	Break-up upon collision of two ice particles (Phillips et al., 2017a). The rimed fraction of the ice crystal and snow particle that undergoes break-up is set to 0.2.
BR0.4	Break-up upon collision of two ice particles (Phillips et al., 2017a), with the rimed fraction for ice crystals/snow set to 0.4.
BRrf	Break-up upon collision of two ice particles (Phillips et al., 2017a), with a diagnostically varying rimed fraction.
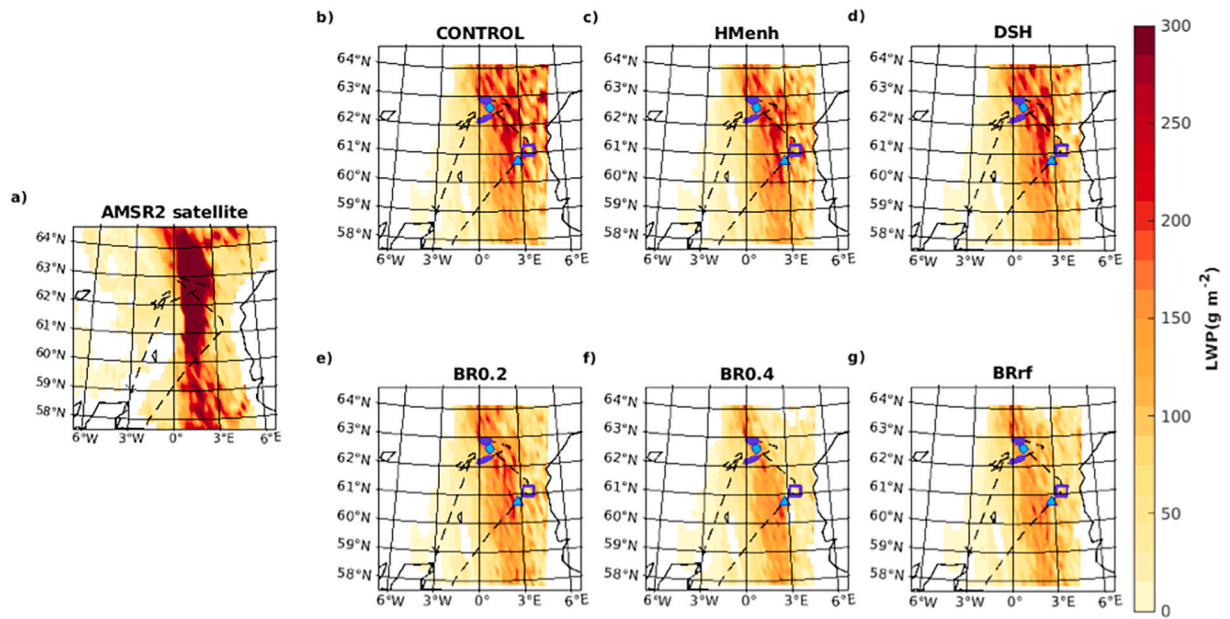
Fig. 4. Liquid water path (LWP) maps from a) AMSR2 satellite observations from overpasses at 1154 and 1336 UTC and b–g) simulations at 1200 UTC. Modeled LWP values are derived from domain D03, averaged over an approximately 13 km × 27 km area to match the 0.25° × 0.25° resolution of the AMSR2 data. Blue dots mark the location of the 10 × 10 km^2 averaging area used for the mean vertical profiles in Figs. 2–3, while dashed black lines indicate the flight track. Purple boxes are used for cloud and decoupling statistics in Sections 4.2 and 4.3. (For interpretation of the references to colour in this figure legend, the reader is referred to the web version of this article.)

LWC profile (Fig. 2f). This simulation also produces a more realistic q_T shape with rapidly decreasing values above 1 km (Fig. 2e). However, BR0.4 underestimates IWC (Fig. 3d), producing similar ice content to CONTROL simulation. The rest of the sensitivity simulations produce larger IWC values, but N_{ice} values peak at much higher altitudes compared to the observed profiles (Fig. 3f). A more realistic N_{ice} profile is produced by BR0.4 in terms of shape, although absolute values remain underestimated.

Fig. 3f suggests that all sensitivity simulations successfully intensify the production of precipitating particles compared to CONTROL, as indicated by the increased N_{d100} values in the cumulus region (Fig. 2h), reaching almost ~1 L^{-1} in DSH, BRrf and BR0.4 simulations. However, N_{d100} concentrations remain underestimated in all tests at the examined location. N_{d100} concentrations are generally dominated by ice particles in the cumulus regime, while the presence of liquid drops is more prevalent in the lowest half kilometer of the atmosphere, obviously due to melting of ice precipitation. Activation of all mechanisms (including a more efficient Hallett-Mossop) simultaneously results in similar thermodynamic and cloud morphology (Figs. S2–3) as in BR runs, suggesting that break-up is the most important mechanism in our simulations.

Our simulations reveal that the initiation of the two SIP processes that are not included in the standard microphysics scheme, drop-shattering and collisional break-up, is clearly favored in the examined conditions. BR0.4 is the only simulation that improves both N_{ice} and N_{d100} profile in the stratocumulus region, but at the same time results in degraded LWC representation. The LWC depletion in BR0.4 could potentially be attributed to the fact that the enhanced concentrations of secondary ice particles increase the efficiency of the Wegener–Bergeron–Findeisen (WBF) mechanism. In the cumulus region both break-up and drop-shattering can substantially impact the modeled number concentrations. Changes in the Hallett-Mossop treatment have also a notable effect on IWC, N_{ice} and N_{d100}. However only break-up of highly rimed particles can reproduce the observed SCT location and thus cloud morphology in the cumulus regime.

The difference in the dynamic properties of the stratiform and cumuliform clouds is also only evident in BR0.4, which produces in-cloud $w_{max} = 0.86$ m s^{-1} and $w_{max} = 1.69$ m s^{-1}, respectively. These

values are in good agreement with the observed (0.87 m s^{-1} and 1.82 m s^{-1}). In contrast, CONTROL produces more similar w_{max} values within the two cloud regimes: 1.98 m s^{-1} and 2.06, respectively. However, it is worth noting that while $(w_{sc})_{max}$ is more realistic in BR0.4 than in CONTROL simulation, the stratocumulus LWC is underestimated in the former and well-reproduced in the latter. This suggests possible over-estimation of the cloud-driven turbulence due to cloud-radiative cooling. The larger maximum vertical velocities in CONTROL simulation also correspond to higher maximum supersaturations over liquid (s_{lmax}) and over ice (s_{imax}) in CONTROL than in BR0.4 simulation. CONTROL produces a s_{lmax} of 0.8% and s_{imax} of 16% in both regimes. BR0.4 produce slightly different values, with s_{lmax} (s_{imax}) increasing from 0.4%(14%) to 0.5%(15%).

Tornow et al. (2021) recently showed that the presence of frozen hydrometeors, mostly in the form of snow, can accelerate the SCT transition. This is in agreement with our findings as BR0.4, the only simulation that produces relatively large ice particles upwind from the observed SCT location (Fig. 3b, c), produces cloud break-up on time; all the other simulations sustain overcast conditions within the observed cumulus regime (Fig. 2f). Tornow et al. (2021) suggest that snow formation affect cloud evolution through a series of riming-related effects that include faster cloud liquid and CCN depletion and onset of light ice precipitation that stratifies the PBL through sublimation/evaporation. The impacts of the enhanced ice formation through SIP on other microphysical processes (including riming), precipitation and PBL structure in Sections 4.3 and 4.4.

4.2. Cloud properties

Fig. 4 shows the simulated horizontal distribution of LWP. The shown modeled LWP values are spatially averaged over an approximately 13 km × 27 km area to match the resolution of the AMSR2 measurements. Satellite observations indicate a clear distinction between the stratocumulus and cumulus regimes, with stratiform LWP values being larger than 300 g^{-2} and cumulus values being generally lower than 200 g^{-2} (Fig. 4a). The CONTROL simulation produce similar LWP values for the two regimes, while cloud break-up is displaced

further downwind than the observed by the aircraft location, which is around the 2.5° meridian at latitudes between 60°N and 62°N (Fig. 4a).

The inclusion of the enhanced H-M mechanism and droplet shattering (Fig. 4c–d) results in a more defined break-up of the cloud layer in the convective region and more realistic LWP values. However, this improvement was less pronounced in a sensitivity test (not shown) with somewhat higher size thresholds in the estimation of the shattering probability (80/100 μm instead of 50/60 μm, see Section 3.2), suggesting that DSH efficiency is sensitive to these parameters. In the sensitivity tests where the collisional break-up process is included (Fig. 4e–g) there is an evident distinction in the stratocumulus and the cumulus regimes, that better conforms with the satellite LWP patterns, especially in the BR0.4 simulation (Fig. 4f). Also, BR runs tend to shift the SCT to the west of the corresponding SCT location in CONTROL, HMenh and DSH simulations, which is in generally better agreement with aircraft observations. All simulations, and especially BR runs, substantially underestimate the stratiform LWP values compared to satellite measurements. However satellite-retrieved LWP in the sampled (by the aircraft) stratocumulus region is generally higher compared to the mean in-situ observations (Fig. 5a). Activating all SIP mechanisms simultaneously results in similar LWP patterns as in BR runs, but with somewhat improved cumulus LWP values for simulations with a low or diagnostic rimed fraction (Fig. S4).

Fig. 5 shows the relative frequency distributions (RFDs) for LWP and number concentrations for particles larger than 100 μm. Modeled stratiform values are averaged over 10×10 km^2 boxes along the aircraft trajectory at longitudes lower than 0.8°E, where profiles of stratocumulus layers were sampled (profiles P1, P2, P5 and P6 in figure 2 of Abel

et al., 2017). Note that modeled LWP here is substantially higher than the values presented in the previous figure; this is because LWP values in Fig. 4 have been averaged over a 13 km $\times$ 27 km area for consistency with the AMSR2 resolution. The LWP model results presented in Fig. 5 correspond to the default 1-km resolution.

Since most simulations fail to reproduce the observed SCT location (Figs. 2, 4), the modeled LWP values along the aircraft trajectory in the observed cumulus regime are not representative of cumulus conditions (Fig. 2). For this reason, to investigate the impact of SIP on cumuliform clouds, we utilize modeled profiles well-located within a 40×40 km^2 area in the cumulus region (see purple box round 3.2°E in Fig. 4). The utilized data are compared to LWP measurements of the MARSS instrument collected along the flight track, while the AMSR2 LWP value that corresponds to the satellite grid that encompasses the selected sample is also shown.

Fig. 5a depicts the relative frequency distribution (RFD) of the stratiform LWP values. All modeled distributions peak at LWP values below 100 g^{-2}, while observations exhibit a broad peak between 50 and 350 g^{-2}, suggesting more variable cloud conditions. All simulations produce similar RFD shapes, underestimating (overestimating) the frequency of LWP values between 300 and 400 g^{-2} (below 100 g^{-2}), except for BRrf which underestimates all LWP values larger than 300 g^{-2}. When the mean LWP values are calculated, the underestimated frequency of low LWPs is balanced by an overestimation of high (>500 g^{-2}) values in CONTROL and DSH simulation, resulting in a 210–215 g^{-2} mean value which is consistent with mean in-situ observations. All other simulations produce mean LWP values below 200 g^{-2}, underestimating the in-situ observed mean by 40–60 g^{-2}. Largest underestimations are produced
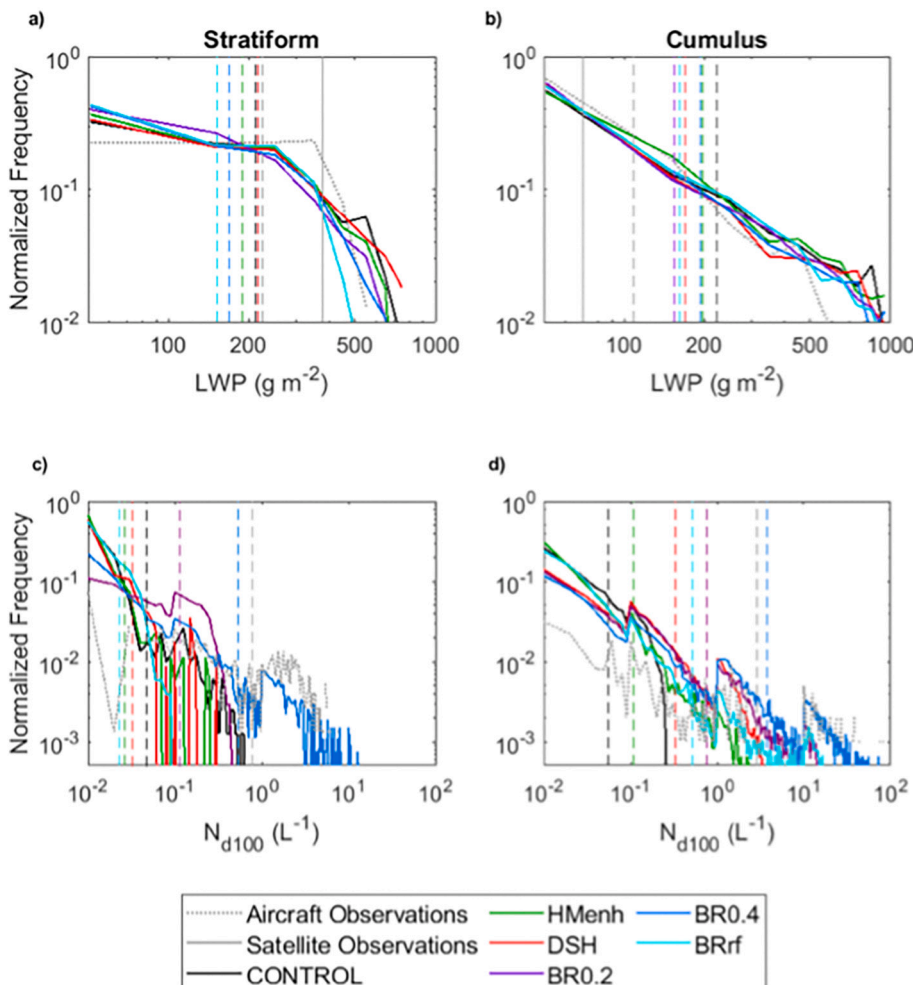

Fig. 5. Relative frequency distribution (RFD) of (a, b) liquid water path (LWP) and (c, d) number concentrations of particles with sizes larger than 100 μm (N_{d100}), calculated (a, c) over 10×10 km^2 boxes along the stratocumulus flight track and (b, d) in a 40×40 km^2 box within the cumulus regime (indicated in Fig. 4) at 1030 UTC and 1200 UTC, respectively. Cloud-free conditions (LWP < 1 g^{-2}) and number concentrations <0.01 L^{-1} are excluded from the analysis. RFDs of LWP are calculated in 100 g m^{-2} bins, while variable bin length is used for the RFDs of N_{d100}. Vertical dashed lines in all panels indicate the mean value. Vertical solid grey lines in panels (a, b) indicate the AMSR2 LWP value in the satellite grids that encompass the utilized samples. Observational curves correspond to data collected along the aircraft trajectory with the MARSS instrument (a,b) and the CIP-100 probe (c, d) before and after the transition. Logarithmic scale is applied to both axes in all panels.

by simulations with active collision break-up, which produce mean LWPs between 150 and 170 g^{-2}. Cloud-free conditions (LWP <1 g^{-2}) are excluded from these statistics. Such conditions are identified in 16–20% of the examined stratocumulus area in CONTROL, DSH, HMenh and BR0.2 simulations, while this percentage increases to 29–30% BRrf and BR0.4. Discontinuity within the stratocumulus layer is neither supported by aircraft measurements, which sampled 100% cloudy conditions, nor by satellite observations, which reveal the presence of a dense cloud deck (Fig. 4a). Satellite-retrieved stratiform LWPs are generally ≥300 g m^{-2} (Fig. 4, 5a), substantially larger than the observed in-situ measurements.

All simulations produce similar frequency of LWP values <200 g^{-2} within the cumulus region (Fig. 5b), except HMenh which produces somewhat enhanced frequencies, in better agreement with in-situ observations. However, the frequency of larger (>500 g^{-2}) values is overestimated in all simulations. This overestimation results in a positive bias in mean LWP, with CONTROL simulation producing the largest mean value at 222 g^{-2}, almost twice as large compared to the in-situ observed mean (108.5 g^{-2}) and three times compared to the satellite value (70 g^{-2}). Cloud-free occcurence in this simulation increases to 33% compared to the stratiform region. Only 19% of the observations indicate clear-sky in the cumulus regime, however research aircraft generally aims to fly through cloudy conditions. Moreover, fewer samples (314) have been collected within the cumulus clouds, compared to the stratocumulus regime (1223).

HMenh produces a decreased mean cumulus LWP of 194 g^{-2}, closer to the observed value, and a cloud-free frequency of 28%. The cloud field excessively dissipates in BR0.4, with cloud free conditions covering 70% of the examined cumulus region. However, within the cloudy patches of this run overestimated LWP values persist, resulting in a mean LWP at 193 g^{-2}. DSH and BRrf also result in excessive cloud break-up with a cloud-free occurrence of 39% and 42%, respectively, in the examined area, but produce an improved mean LWP (170 g^{-2} and 161 g^{-2}) compared to BR0.4. BR0.2 gives the most optimal LWP results in the cumulus region with a mean LWP (153 g^{-2}) that is closer to the observed than any other simulation and a cloud-free frequency of 44%.

RFDs of N_{d100} reveal a general underestimation of the observed stratocumulus particle concentrations (>100 μm) in all simulations except for BR0.4 (Fig. 5c). Larger concentrations are produced by the simulations with active break-up. BR0.4 produces the most realistic range of N_{d100} values and a mean N_{d100} close to the measured one (Fig. 5c). BR0.2 produces a narrower range of values compared to BR0.4, underestimating the frequency of N_{d100} values >1 L^{-1}, and a mean N_{d100} around 0.2 L^{-1}. All the other simulations produce mean values below 0.1 L^{-1}, thus more than one order of magnitude lower than the observed mean.

Most simulations show a pronounced increase in number concentrations in the cumulus region (Fig. 5d), compared to the stratiform (Fig. 5c), except for CONTROL which produces similar mean concentrations in both regimes. The CONTROL simulation does not produce any values larger than 0.5 L^{-1}, which results in a significantly underestimated mean value for the cumulus conditions (Fig. 5d). The results are improved with the HMenh set-up, which produces N_{d100} values larger than 1 L^{-1}, but mean N_{d100} remains substantially underestimated compared to the observed. DSH and especially BR simulations give a more realistic representation of the observed N_{d100} range in the cumulus regime, with BR0.4 being the simulation that produces a mean N_{d100} value very close to the observed (Fig. 5d). Cloud properties for simulations that account for all SIP mechanisms (Fig. S5) produce very similar results to BR runs in the cumulus region.

It is worth noting that apart from SIP, the description of which remains incomplete in atmospheric models, primary ice production parameterizations are also source of great uncertainty for cloud representation. Primary ice concentrations in the CONTROL simulation is of the order of 0.1–0.2 L^{-1}. Heterogeneous freezing in the Morrison scheme is parameterized using some relatively old numerical

descriptions: immersion and condensation freezing are parameterized following Bigg (1953) and Meyers et al. (1992), respectively, while the description developed by Cooper (1986) is adapted for deposition/condensation freezing. However, multiplying the predicted primary concentrations by a factor of 10 had a weak impact on the concentrations of the relatively large particles (N_{d100}) (not shown). This was also the case with a sensitivity test in which the DeMott et al. (2010) parameterization replaced the one developed by Cooper (1986) (not shown). These results suggest that uncertainties in SIP are likely more important than uncertainties in primary ice parameterizations for the representation of the precipitation patterns.

4.3. SIP impacts on other microphysical processes

Activation of additional SIP mechanisms in the model has very pronounced impacts on the modeled cloud macro- and micro- physical properties (Section 4.2). To understand the underlying interactions of SIP with other microphysical processes we show mean tendency profiles for SIP, riming, cloud ice depositional and snow aggregation (Fig. 6) for the stratocumulus and cumulus regimes studied in Section 4.2 (purple boxes in Fig. 4).

The SIP tendencies of the stratocumulus clouds are largest in BR0.2 and BR0.4 simulations (Fig. 6a). DSH and BRrf produce very weak SIP (<0.001 L^{-1} s^{-1}), while HMenh produces significant SIP only a narrow atmospheric layer that satisfies the temperature criteria for this mechanism. In the cumulus regime (Fig. 6b) all SIP tendencies become substantially enhanced, with SIP production being at least 1.5–2 orders larger in BR0.4 than in any other simulation at the same atmospheric level. It worths noting that while the Hallet-Mossop mechanism is activated in both cloud regions in HMenh run, this is not the case for CONTROL which does not produce any SIP in the stratocumulus region (Fig. 6a). This suggests that stratiform clouds generally consist from smaller liquid and ice particles that do not meet the size criteria adapted in the default Hallett-Mossop parameterization (see Section 3.2). In the cumulus regime, CONTROL and HMenh produce very similar tendencies, with somewhat weaker SIP rates in the later (Fig. 6b). We believe that enhancing the efficiency of this mechanism results in faster depletion of the available liquid that is then available to continue feeding ice multiplication. This is also indicated by the somewhat lower LWP values in HMenh compared to CONTROL (Fig. 5a).

Interestingly, increasing SIP has marginal impacts on riming (Fig. 6c). The two simulations with substantial SIP production in the stratiform regime are also characterized by enhanced riming. In contrast, the HMenh, DSH and BRrf simulations, with limited SIP efficiency, result in even weaker aggregation rates. SIP generally can result in: (a) larger number of ice particles that can increase the frequency of ice-liquid collisions and thus riming probability, and (b) smaller ice particles that are less efficient in riming. Note that BR0.2 and BR0.4 are the only simulations that produce larger N_{d100} concentrations than CONTROL (Fig. 5c), while the rest of the simulations generally produce smaller particles (<100 μm) which is consistent with the decreased riming efficiency observed in Fig. 6c. Riming becomes more pronounced in the cumulus regime in all simulations, with BR0.4 simulation producing substantially higher rates than any other set-up (Fig. 6d).

Panels e–f show the depositional growth rates for the cloud ice category. In the stratocumulus regime only BR simulations produce significant cloud ice deposition, which is in agreement with the overall decreased LWP values in Fig. 5a. These tendencies become substantially larger in the cumulus regime for all simulations, except CONTROL. CONTROL is the only simulation that produces a mean $N_{d100} < 0.01$ L^{-1} (Fig. 5d), thus does not include many large enough ice particles than can compete effectively with liquid droplets for the available water vapor. This also explains why CONTROL simulation sustains the highest LWP values in the cumulus regime (Fig. 5b). The cloud-ice to snow autoconversion rates are very similar to those for depositional growth and this is why they are not shown in Fig. 6. This is because only the cloud
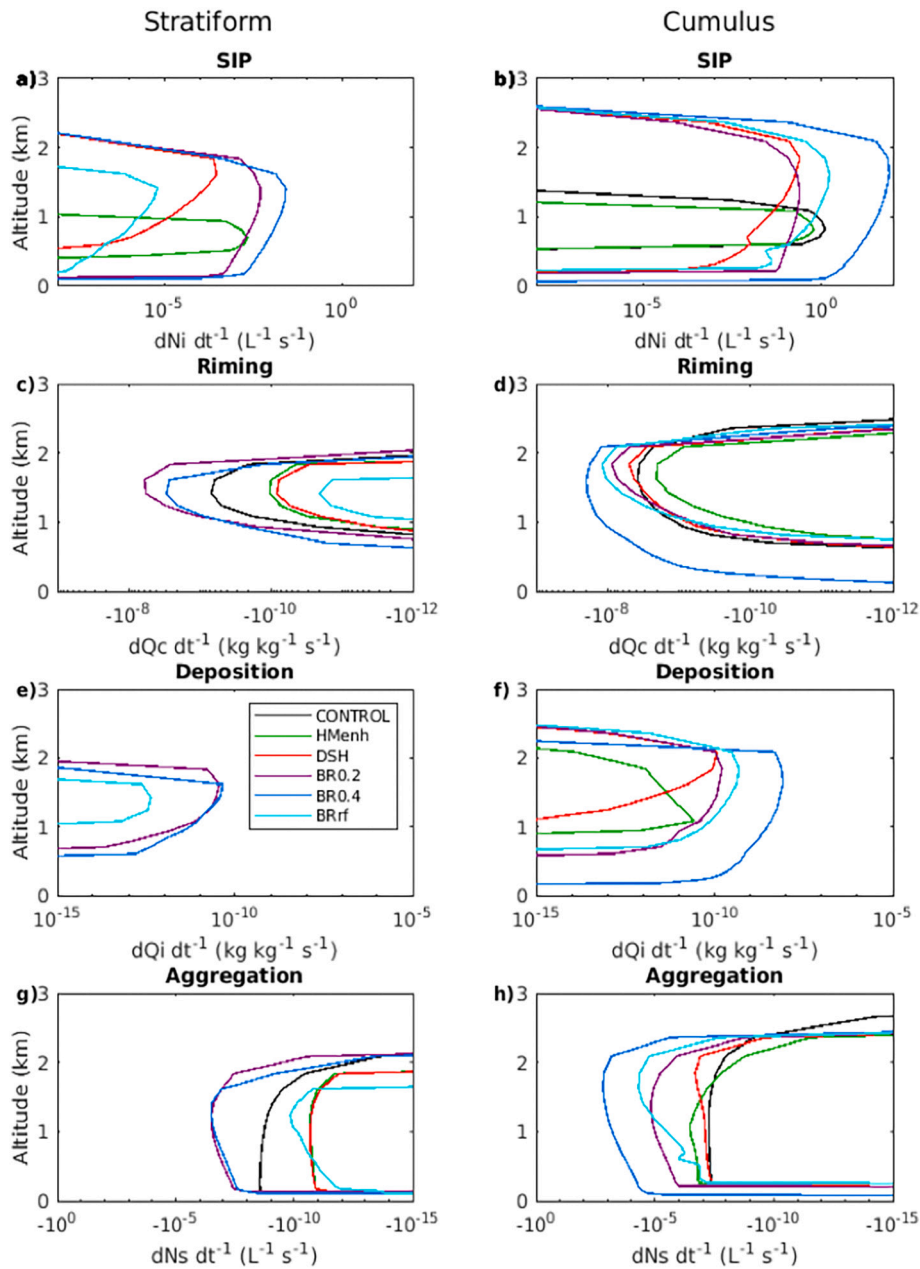
Fig. 6. Vertical profiles of (a, b) ice number tendency due to SIP, (c, d) cloud liquid mass change due to riming, (e, f) cloud ice mass growth due to vapor deposition and (g, h) snow number concentration decrease due to aggregation. All mean tendencies are averaged (a, c, e, g) over 10×10 km^2 boxes along the stratocumulus flight track and (b, d, f, h) in a 40×40 km^2 box within the cumulus regime (indicated in Fig. 4) at 1030 UTC and 1200 UTC, respectively.

ice particles undergone significant depositional growth can turn into snowflakes, further enhancing the precipitation-size particle concentrations.

Snow aggregation behaves similarly to riming in the stratocumulus regime (Fig. 6g), being enhanced (depleted) in BR0.2 and BR0.4 (HMenh, DSH, BRrf) compared to CONTROL simulation. The explanation is likely the same as for the riming tendency and is related to the fact that only BR0.2 and BR0.4 produce larger N_{d100} concentrations (which include snow) than CONTROL (Fig. 5c), thus snow particles large enough to trigger aggregation. The aggregation rates become substantially larger in the cumulus regime for all sensitivity simulations except for CONTROL (Fig. 6h). Small enhancements in snow aggregation are produced by DSH and HMenh compared to CONTROL, while this process is substantially favored in BR simulations, which produce more than two order of magnitudes larger tendencies compared to the standard

model version. Cloud-ice aggregation exhibits a very similar behaviour as vapor deposition (not shown in Fig. 6). This is again because only cloud ice particles with significant mass growth can contribute to aggregation and form snow.

In summary, changes in SIP treatment can have a substantial on the efficiency of other microphysical processes, such as riming, deposition growth, snow autoconversion and aggregation. Overall, a substantial increase in SIP production results in enhanced riming, and thus graupel formation. Another consequence is an enhancement in cloud-ice depositional growth and thus cloud ice-to-snow autoconversion and cloud ice aggregation, leading to more snow formation. This is particularly evident in BR0.4 simulation where all these microphysical processes appear more effective than in any other simulation. The enhanced formation of precipitation-sized particles, like graupel and snow, in BR0.4 likely accelerates the onset of heavy precipitation, which explains why

the SCT happens further west (upwind) than in any other sensitivity test. This is in general agreement with Tornow et al. (2021) who found that increasing ice number concentration can accelerate cloud break-up through a series of riming affects (although aggregation also plays an important role in our simulations).

4.4. PBL decoupling

Boundary-layer decoupling is a fundamental component of the SCT theory and has been frequently observed in marine PBLs (Paluch and Lenschow, 1991; Yin and Albrecht, 2000; Rémillard et al., 2012; Jones et al., 2011; Dong et al., 2015). The most widely-applied methodology for the identification of PBL decoupling in the literature (e.g. Yin and Albrecht, 2000; Rémillard et al., 2012; Jones et al., 2011; Dong et al., 2015) is the use of conserved thermodynamic variables, such as ice-liquid potential temperature (θ_{il}) and total mixing ratio (q_T). This is because the "coupled state" implies that these variables are vertically well-mixed within the PBL. On the contrary, positive gradients within the PBL indicate the presence of two layers with different thermodynamic conditions, suggesting lack of interaction/mixing.

Here, we utilize $\Delta\theta_{il}$ (approximated as $\theta_{il} = \theta - (L_v/C_p)q_l - (L_s/C_p)q_i$) and Δq_T to assess the occurrence and intensity of decoupling, which are defined as the ice-liquid potential temperature and total water content difference between the upper and lower quartiles of the boundary layer, using the cloud top height to identify the PBL top. $\Delta\theta_{il} < 0.5\ °C$ and $\Delta q_T < 0.5\ g\ kg^{-1}$ correspond to a well-mixed vertical structure, while $\Delta\theta_{il} > 0.5\ °C$ and $\Delta q_T > 0.5\ g\ kg^{-1}$ indicate a poorly-mixed profile (Jones et al., 2011; Abel et al., 2017), with q_T being accumulated near the surface due to the possible formation of a temperature inversion within the PBL. The decoupling metrics for the main simulations are shown in Fig. 7, while for the complementary runs, that account for all SIP mechanisms, are

offered in Fig. S6. These are derived from the areas indicated with purple boxes in Fig. 4.

Aircraft measurements show a clear distinction between the stratocumulus and cumulus region (Fig. 7), with stratocumulus profiles exhibiting a homogeneous vertical PBL structure. All measured cumulus profiles appear to be decoupled, characterized by $\Delta\theta_{il} > 2\ °C$ and $\Delta q_T > 1\ g\ kg^{-1}$. In the CONTROL simulation (Fig. 7a), the stratocumulus profiles are predominantly well-mixed, while in the cumulus region a large number of profiles appear to be decoupled, but not to the degree shown by the measurements. HMenh and BRrf demonstrate minor improvements in their predictions (Fig. 7b, f), slightly reducing the difference between the simulated and observed metrics of the decoupled cumulus profiles. Profiles with decoupling intensity comparable to the observed are only produced by the DSH, BR0.2 and BR0.4 simulations (Fig. 7c, d, e). Activation of all SIP mechanisms simultaneously results in somewhat further enhancement of PBL stratification in the cumulus regime (Fig. S5).

In the previous section we found that increasing SIP results in enhanced formation of precipitation-sized particles through enhanced depositional growth, aggregation and riming. To further examine the impacts of SIP, precipitation and PBL structure on the initiation of the SCT, we study the temporal evolution of the air masses in a Lagrangian framework, as they cross from the stratiform to the convective region (Figs. 8, 9). To quantify the respective influence of drop-shattering and break-up, we focus on DSH and BR0.4 simulations. BR0.4 is selected for this analysis, since it is more successful in reproducing the observed SCT location than any other simulation that employs this SIP mechanism (Figs. 2–4). Each trajectory is calculated using the wind velocity and wind direction values below 1.5 km, following the same methodology as in Abel et al. (2017). It consists of 32 grid points and is initialized at 0500 UTC, starting at 0.79°E, 63.8°N and ending at the southern edge of
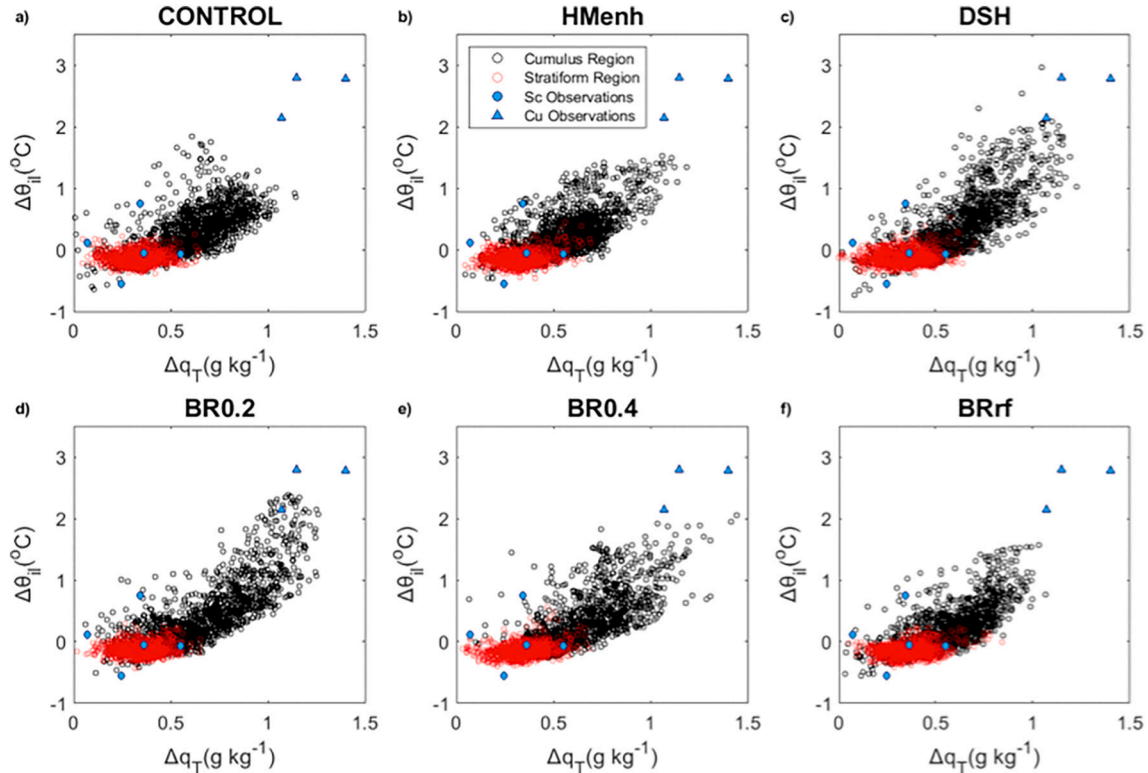

Fig. 7. Decoupling metrics derived from $10 \times 10\ km^2$ boxes along the stratocumulus flight track (red) and in a $40 \times 40\ km^2$ box within the cumulus regime (black) at 1030 UTC and 1200 UTC, respectively (see purple boxes in Fig. 4). $\Delta\theta_{il}$ and Δq_T correspond to the ice-liquid potential temperature and total water content difference between the upper and lower quartiles of the boundary layer (cloud top height is used to approximate PBL top in the calculations). Blue dots and triangles represent cloud profiles as measured by the aircraft in the Stratocumulus and Cumulus region, respectively. (For interpretation of the references to colour in this figure legend, the reader is referred to the web version of this article.)
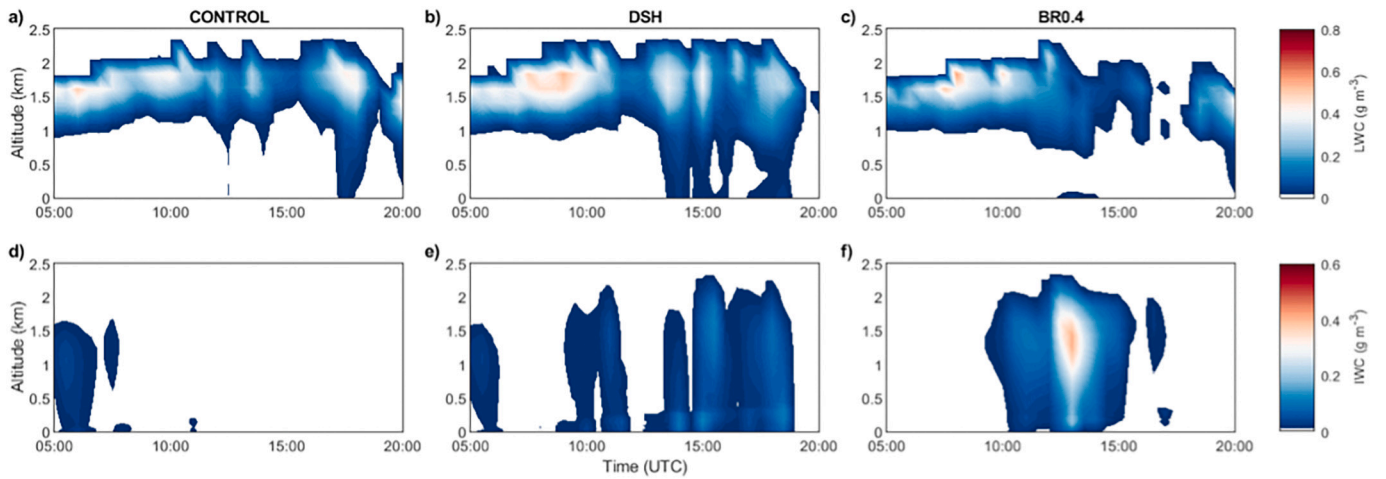
Fig. 8. Time-height cross-section of (a–c) liquid (LWC) and (d–f) ice (IWC) water content along the air-mass forward trajectory. Values are averaged over 10×10 km^2 areas that surround each trajectory grid point.
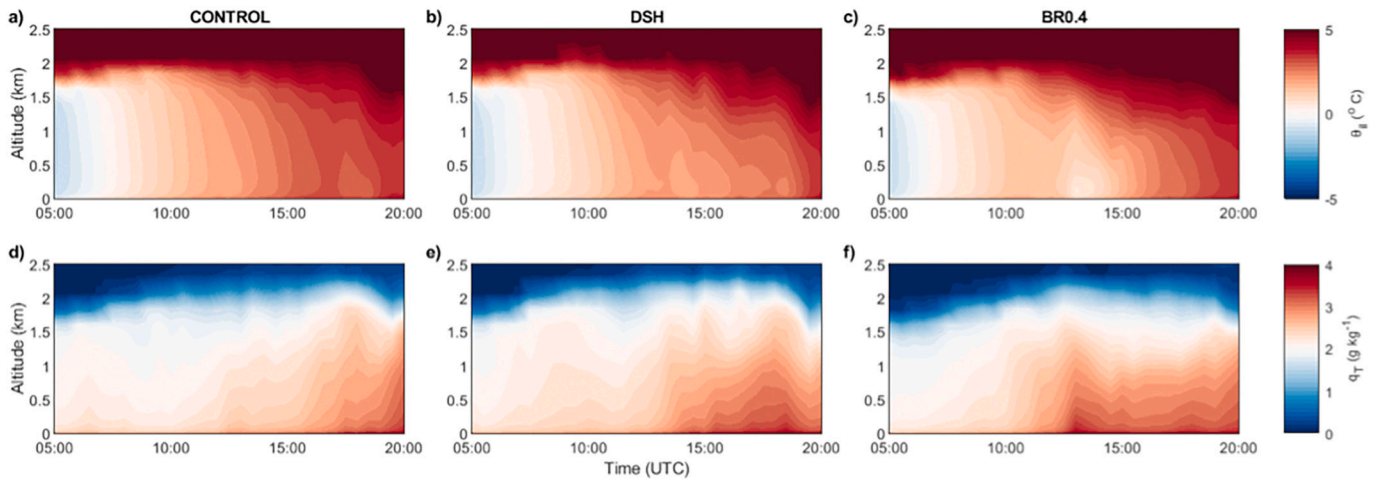

Fig. 9. Same as Fig. 8, but for (a–c) ice-liquid potential temperature (θ_{il}) and (d–f) total water mixing ratio (q_T).

the innermost domain, crossing through the aircraft measurement site. The microphysical and thermodynamic values presented in Figs. 8 and 9 are averaged over 10×10 km^2 boxes with centers taken along the trajectory.

All simulations show a similar initial state of a mostly continuous stratocumulus cloud, with LWC values close to 0.4 g^{-3}. After 1600 UTC the enhanced surface fluxes result in a deeper and optically-thicker cloud in the CONTROL simulation (Fig. 8a), which starts generating liquid precipitation around 1700 UTC. The onset of precipitation is accompanied by the formation of a stable layer, almost 1 km deep above the surface and a notable accumulation of q_T below the temperature inversion (Fig. 9a, d). This cloud almost dissipates around 1900 UTC, while a lower cumulus layer immediately appears. Weak ice precipitation is only generated by the stratocumulus layer around 0500 UTC, at the most northern point of the trajectory (Fig. 8d).

Activation of DSH results in the enhancement of ice precipitation (Fig. 8e), especially from 1350 UTC and onward, with IWC reaching values as high as 0.2 g^{-3}. Liquid precipitation is also enhanced in this simulation compared to CONTROL (Fig. 8a, b), likely due to melting of the frozen hydrometeors in the sub-cloud layer. The simultaneous presence of ice and liquid precipitation heavily impacts the PBL structure, with θ_{il} and q_T cross-sections exhibiting prominent vertical gradients (Fig. 9b, e), indicating decoupling, followed by a clear breaking of the cloud layer near the end of the trajectory. In BR0.4, ice precipitation

is intensified (Fig. 8c,f) with IWC reaching 0.4 g m^{-3} at 1300 UTC and the stratocumulus cloud dissipating completely a few hours later, at 1600 UTC. The enhanced ice precipitation coincides with the formation of a strong temperature inversion (Fig. 9c) and q_T values rapidly decreasing with height (Fig. 9f). The θ_{il} profiles both upwind and downwind of the location of precipitation are more well-mixed (Fig. 9c).

Our simulations indicate a clear correlation between precipitation, PBL decoupling and cloud break-up, in agreement with previous studies that highlighted the importance of evaporation/sublimation of precipitation for the onset of SCT (Paluch and Lenschow, 1991; Abel et al., 2017; Yamaguchi et al., 2017; Tornow et al., 2021). This occurs because precipitation evaporation leads to near-surface cooling that stabilizes the lower atmosphere. This in turn inhibits upward surface fluxes – which decouples the stratiform cloud from the moisture supply required to sustain it and promotes its breakup. Note that the cooling from the evaporation could have a destabilizing effect if the precipitation evaporates higher before reaching the surface layer. However, when the evaporation extends down to the surface this drives stabilization (Fig. 9c), inhibiting upward moisture transport (Paluch and Lenschow, 1991). This results in a near-surface moisture and heat buildup that can eventually lead to convective instability and cumuli formation (Paluch and Lenschow, 1991; Stevens et al., 1998).

Increasing SIP results in enhanced ice precipitation and more rapid decoupling, which accelerates cloud break-up. Collisional break-up is

likely more efficient than drop-shattering in the studied conditions, however the efficiency of the former largely depends on the treatment of rimed fraction. Finally, it should be mentioned that while observations indicate the development of a cumulus layer below the stratocumulus deck before the dissipation of the latter (Abel et al., 2017), this is not captured by any simulation (Fig. 8). An analysis of several trajectories with different starting locations (not shown) revealed that generally the model does not reproduce such multi-layer cloud structures, independently of the treatment of SIP.

4.5. The impact of particles' terminal velocities on SIP

As concluded above, the modeled SIP effects on SCT occur mainly through the enhancement of ice precipitation. However precipitation patterns are influenced by uncertainties in other microphysical processes as well, such as sedimentation. In this section we examine whether changes in the particles' terminal velocities can result in a similar acceleration of the onset of precipitation as caused by drop-shattering and collisional break-up (Fig. 8). In the Morrison scheme, terminal velocity (v) is a function of diameter (D), $v = a\,D^b$, where a and b are highly uncertain parameters. Uncertainties in v not only have a direct impact on precipitation rates but also affect particle collision rates and SIP efficiency (note that drop-shattering and collisional break-up descriptions are functions of collisional kinetic energy).

In the first set of sensitivity simulations we decrease the terminal velocities of all precipitating hydrometeor categories (rain, cloud ice, graupel and snow) by a factor of two; the corresponding results are shown in Fig. 10. The reduced fall velocities result in increased LWP, compared to Fig. 4, over the whole domain. Similarly to Fig. 4, CONTROL, HMenh and DSH fail to reproduce well-defined stratocumulus and cumulus regimes, with pronounced spatial LWP gradients. Moreover, in the new set of simulations, LWP gradients become even weaker in BR0.2 and BRrf. Again BR0.4 is the simulation with the most prominent distinction between the stratiform and the cumulus regimes, in better agreement with satellite observations.

In the second set of sensitivity simulations we increase all fall velocities by a factor of two (Fig. 11). This results in increased precipitation and thus decreased LWP over both cloud regimes in all simulations. However, the representation of SCT did not improve in CONTROL, HMenh and DSH, which sustain similar LWP values over both stratocumulus and cumulus regions. The LWP reduction is even more pronounced in BR simulations, which leads to enhanced break-up of the stratocumulus clouds, compared to Fig. 4. As a result, in this set of simulations BR0.4 performance gets worse, as this set-up produces a less extensive stratocumulus layer that almost dissipates above 62°N. BR0.2 and especially BRrf, with somewhat larger LWP values, are now in better agreement with satellite measurements.

Our results suggest that the impact of SIP, and particularly of collisional break-up, on SCT cannot be compensated by changes in precipitation rates through the adjustment of terminal velocity parameters. However the effect on SIP efficiency from the prescription of a high rimed fraction can be compensated by an increase in fallspeed parameters (while a lower rimed fraction is assumed). This suggests that other microphysical uncertainties in the representation of the hydrometeors' properties can be of similar importance as rimed fraction for the description of SIP effects in models. Finally, it is worth noting that changes in terminal velocities reflect different timescales for hydrometeor settling, but do not account for changes of supersaturation driving evaporation/sublimation in downdrafts of a few hudred meters scale. The microphysics of stratocumulus mixed-phase clouds has been shown to be largely determined by these smaller-scale eddies (Khain et al., 2022), however these cannot be resolved by mesoscale models.

5. Discussion and conclusions

This study examines the impact of three SIP mechanisms, Hallett-Mossop, drop-shattering and break-up upon ice-ice collisions on a SCT during a cold-air outbreak observed north of UK in 2013. Investigations are performed with the WRF model and the updated Morrison microphysics scheme that includes descriptions for all three mechanisms (Sotiropoulou et al., 2021a; Georgakaki et al., 2021).

The default model version fails to reproduce the location of the SCT, as indicated by aircraft observations. Although it gives a realistic representation of stratocumulus liquid properties, it overestimates liquid content in the cumulus regime. Moreover, it substantially underestimates number concentrations of particles larger than 100 μm in all cloud types. In reality Hallett-Mossop requires the presence of liquid droplets smaller than 13 μm and larger than 24 μm (Hallett and Mossop, 1974). However, the activation of Hallett-Mossop in the default Morrison scheme is prevented by thresholds in the liquid and ice mass mixing ratios, which have no physical basis and are rather tuning parameters. Removing these thresholds causes a weak enhancement in the modeled
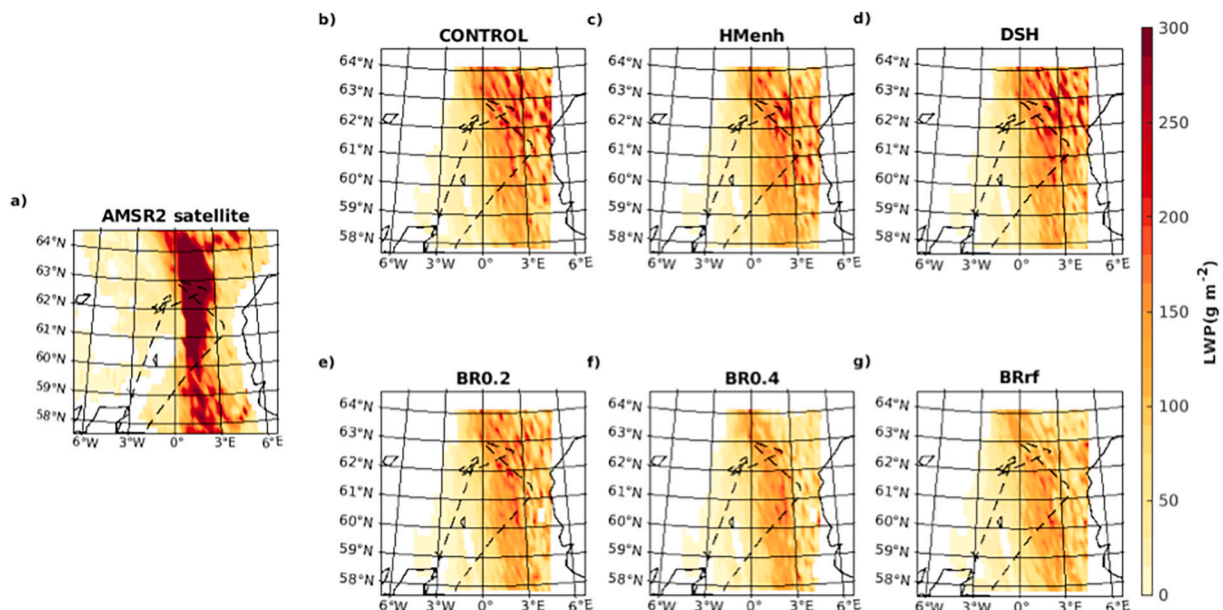

Fig. 10. Same as Fig. 4 but for simulations with precipitating particles' (rain, cloud ice, graupel and snow) terminal velocities decreased by a factor of two.
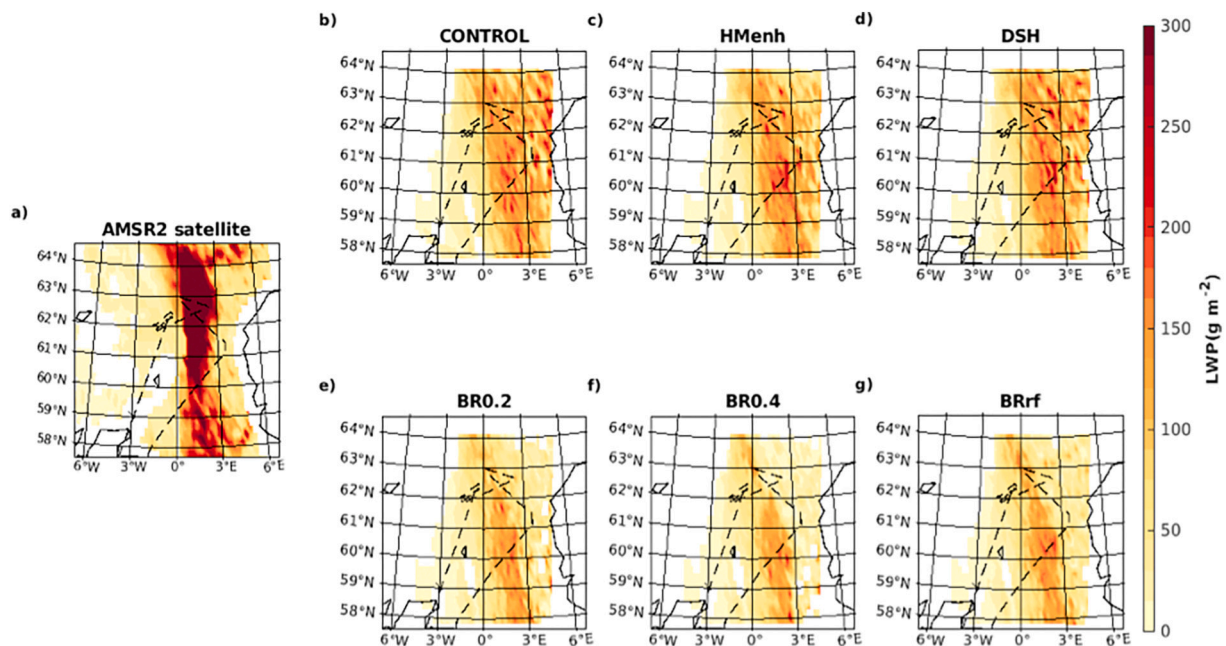
Fig. 11. Same as Fig. 4 but for simulations with precipitating particles' (rain, cloud ice, graupel and snow) terminal velocities increased by a factor of two.

number concentrations, suggesting that this mechanism alone cannot explain observations.

Drop-shattering appears more effective in the examined cumulus conditions compared to Hallett-Mossop, even when no size limitation is considered for the latter. Activation of this mechanism results in significant enhancement of precipitation-sized particles which sublimate in the sub-cloud layer, enhancing cloud decoupling from the surface moisture sources. Yet, when drop-shattering operates alone, it cannot reproduce the observed range of particle number concentrations and accurately predict the observed SCT location. An enhancement in drop-shattering and precipitation efficiency through increases in particles' terminal velocities did not improve the results. However, it should be noted that there are still significant uncertainties in the predictions of the generated fragments, due to poorly constrained parameters in the adapted formulation (Phillips et al., 2018), e.g. such as the frozen fraction of the drops (James et al., 2021).

Collisional break-up is the only SIP mechanism that results in significant ice number enhancement in both stratiform and cumulus regimes. However, the efficiency of this process highly depends on the treatment of rimed fraction for cloud ice and snow. The simulation with highly rimed particles captures the observed SCT location, sampled by the aircraft and also reproduces the observed particle number concentration range. Yet, this run produces excessive break-up and overestimates the frequency of cloud-free conditions. Simulations with a low prescribed rimed fraction reduce this cloud-break overestimation, but produce somewhat lower particle concentrations and do not capture the observed SCT location. Yet, this finding is very sensitive to the treatment of hydrometeor fallspeed parameters; increasing terminal velocities of the precipitating particle categories instead of enhancing the prescribed rimed fraction can have a similar impact on SIP efficiency.

It should be noted that for the implementation of the Phillips et al. (2017a) parameterization for collisional-break-up in the Morrison scheme, a large number of simplifications has been considered. Apart from the simplified treatment of rimed fraction, a constant ice habit is also assumed, while the correction factor for sublimation effects adapted in the (Phillips et al., 2017a) description also consists a great source of uncertainty (Sotiropoulou et al., 2021b). Moreover, bulk microphysics schemes like Morrison et al. (2005) use fixed parameters to categorize frozen hydrometeors in cloud ice, snow or graupel categories, which limits the physical realism of the ice microphysical treatment. Since

fragment generation largely varies for these three hydrometeor types (Phillips et al., 2017a), uncertainties in this categorization approach have direct impacts on the representation of the break-up process. Microphysical schemes that allow for several physical properties to evolve freely in time and space, including rimed fraction (Morrison and Milbrandt, 2015) and ice habit (Jensen et al., 2017), can likely improve the accuracy of the break-up description. WRF, however, does not include schemes that predict ice shape, while the Morrison and Milbrandt (2015) scheme currently accounts for only two ice categories, thus has a very limited ice spectral representation.

Moreover, apart from uncertainties in the studied ice formation processes, it is also possible that other SIP mechanisms, not included in Morrison scheme, might have contributed to the observed high ice number levels. For example, fragmentation of sublimating particles (Oraltay and Hallett, 1989) is a SIP mechanism whose efficiency in real atmospheric conditions remains poorly quantified. The ice fragments formed during sublimation have to re-enter back into supersaturated cloud levels to contribute to ice multiplication. Considering that observations at the SCT location indicate the presence of a stratiform layer over a cumulus cloud, sublimating precipitation particles from the overlying cloud into the cumulus can theoretically initiate this SIP mechanism. However, the model cannot reproduce this two-layer structure.

An open question that remains is whether the presence of a lower cumulus at warmer atmospheric levels in the model, capped by the stratocumulus layer, would have changed the relative importance of the examined SIP mechanisms for PBL decoupling. While Hallett-Mossop would be favored in the sub-cumulus cloud, examination of cumulus profiles within the optimal temperature range and with similar cloud water content as the observed (not shown) revealed that such high number concentrations, as indicated by the measurements, are not reproduced when Hallett-Mossop is the only active SIP mechanism. Thus the contribution of additional mechanisms would still be likely required to reproduce the observed amount of precipitating particles.

Nevertheless, our results indicate that drop-shattering and collisional break-up are favored in the examined conditions and could potentially play a more critical role for the SCT than Hallett-Mossop. This highlights the need for more extensive laboratory studies of these processes to improve existing parameterizations. The utilized descriptions are based on theory and are constrained with very old laboratory experiments

and/or field measurements (Phillips et al., 2017a, 2018). Ongoing laboratory studies of the drop-shattering process (Lauber et al., 2018; Keinert et al., 2020; Kleinheins et al., 2021; James et al., 2021) can substantially improve our understanding of this mechanism and provide better constraints for the fragment generation rate and its dependence on different cloud and atmospheric parameters. However, similar studies are urgently needed for the collisional break-up mechanism, whose efficiency can potentially be of similar or greater importance during CAO events.

Finally, for the more accurate description of SIP in bulk microphysics schemes, better constraints of other microphysical properties, such as terminal velocity and rimed fraction, are also required. A suggestion would be the collection of extensive cloud radar measurements under several cloud conditions for the improvement of the existing fallspeed-diameter relationships (e.g. Radenz et al., 2018), while the different hydrometeor types can be inferred using dual-polarization radars. Furthermore, a parameterization for rimed fraction as a function of temperature and size can be developed based on field measurements; rimed fraction can be inferred from particle images using, for example, the classification method of Mosimann et al. (1994). In particular, Mosimann et al. (1994) classify particles within a 0 to 1 range; 0 represents lack of riming while 5 is for graupels. These values can be scaled to fit the 0–0.5 rimed fraction range in Phillips scheme, where 0.5 represents graupel. The developed parameterization can be then used in bulk microphysics schemes that do not predict this parameter.

Declaration of Competing Interest

The authors declare that they have no known competing financial interests or personal relationships that could have appeared to influence the work reported in this paper.

Acknowledgements

Appendix A. Supplementary data

Supplementary data to this article can be found online at https://doi.org/10.1016/j.atmosres.2022.106302.

References

Abel, S.J., Boutle, I.A., Waite, K., Fox, S., Brown, P.R.A., Cotton, R., Lloyd, G., Choularton, T.W., Bower, K.N., 2017. The role of precipitation in controlling the transition from stratocumulus to cumulus clouds in a Northern Hemisphere cold-air outbreak. J. Atmos. Sci. 74 (7), 2293–2314. https://doi.org/10.1175/JAS-D-16-0362.1.

Atlas, R.L., Bretherton, C.S., Blossey, P.N., Gettelman, A., Bardeen, C., Lin, P., Ming, Y., 2020. How well do large-eddy simulations and global climate models represent observed boundary layer structures and low clouds over the summertime Southern Ocean? J. Adv. Model. Earth Sy. 12 https://doi.org/10.1029/2020MS002205 e2020MS002205.

Baumgardner, D., Brenguier, J.L., Bucholtz, A., Coe, H., DeMott, P., Garrett, T.J., Gayet, J.F., Hermann, M., Heymsfield, A., Korolev, A., Krämer, M., Petzold, A., Strapp, W., Pilewskie, P., Taylor, J., Twohy, C., Wendisch, M., Bachalo, W., Chuang, P., 2011. Airborne instruments to measure atmospheric aerosol particles, clouds and radiation: a cook's tour of mature and emerging technology. Atmos. Res. 102 (1–2), 10–29. https://doi.org/10.1016/j.atmosres.2011.06.021.

Bigg, E.K., 1953. The formation of atmospheric ice crystals by the freezing of droplets. Q. J. R. Meteorol. Soc. 79, 510–519. https://doi.org/10.1002/qj.49707934207.

Bretherton, C.S., Wyant, M.C., 1997. Moisture transport, lower-tropospheric stability, and decoupling of cloud-topped boundary layers. J. Atmos. Sci. 54 (1), 148–167. https://doi.org/10.1175/1520-0469(1997)054<0148:MTLTSA>2.0.CO;2.

Brown, P., Francis, P., 1995. Improved measurements of the ice water content in cirrus using a total-water probe. J. Atmos. Ocean. Technol. 12, 410–414. https://doi.org/10.1175/1520-0426(1995)012<0410:IMOTIW>2.0.CO;2.

Chung, D., Matheou, G., Teixeira, J., 2012. Steady-state large-eddy simulations to study the stratocumulus to shallow cumulus cloud transition. J. Atmos. Sci. 69 (11), 3264–3276. https://doi.org/10.1175/JAS-D-11-0256.1.

Cooper, W.A., 1986. Ice initiation in natural clouds. Meteorol. Monogr. 21, 29–32. https://doi.org/10.1175/0065-9401-21.43.29.

Dedekind, Z., Lauber, A., Ferrachat, S., Lohmann, U., 2021. Sensitivity of precipitation formation to secondary ice production in winter orographic mixed-phase clouds. Atmos. Chem. Phys. 21, 15115–15134. https://doi.org/10.5194/acp-21-15115-2021.

DeMott, P.J., Prenni, A.J., Liu, X., Kreidenweis, S.M., Petters, M.D., Twohy, C.H., Richardson, M.S., Eidhammer, T., Rogers, D.C., 2010. Predicting global atmospheric ice nuclei distributions and their impacts on climate. Proc. Natl. Acad. Sci. 107 (25), 11217–11222. https://doi.org/10.1073/pnas.0910818107.

Dong, X., Schwantes, A.C., Xi, B., Wu, P., 2015. Investigation of the marine boundary layer cloud and CCN properties under coupled and decoupled conditions over the Azores. J. Geophys. Res. Atmos. 120 https://doi.org/10.5194/acp-2021-302.

Field, P.R., Heymsfield, A.J., Bansemer, A., 2006. Shattering and particle interarrival times measured by optical array probes in ice clouds. J. Atmos. Ocean. Technol. 23, 1357–1371. https://doi.org/10.1175/JTECH1922.1.

Field, P., Lawson, P., Brown, G., Lloyd, C., Westbrook, D., Moisseev, A., Miltenberger, A., Nenes, A., Blyth, A., Choularton, T., Connolly, P., Bühl, J., Crosier, J., Cui, Z., Dearden, C., DeMott, P., Flossmann, A., Heymsfield, A., Huang, Y., Kalesse, H., Kanji, Z., Korolev, A., Kirchgaessner, A., Lasher-Trapp, S., Leisner, T., McFarquhar, G., Phillips, V., Stith, J., Sullivan, S., 2017. Chapter 7: secondary ice production - current state of the science and recommendations for the future. Meteorol. Monogr. 58, 7.1–7.20. https://doi.org/10.1175/AMSMONOGRAPHS-D-16-0014.1.

Fletcher, J., Mason, S., Jakob, C., 2016. The climatology, meteorology, and boundary layer structure of marine cold air outbreaks in both Hemispheres. J. Clim. 29 (6), 1999–2014. https://doi.org/10.1175/JCLI-D-15-0268.1.

Georgakaki, P., Sotiropoulou, G., Vignon, É., Billault-Roux, A.-C., Berne, A., Nenes, A., 2021. Secondary ice production processes in wintertime alpine mixed-phase clouds. Atmos. Chem. Phys. Discuss. https://doi.org/10.5194/acp-2021-760 [preprint]. (in review).

Hallett, J., Mossop, S., 1974. Production of secondary ice particles during the riming process. Nat. 249, 26–28. https://doi.org/10.1038/249026a0.

Hersbach, H., Bell, B., Berrisford, P., et al., 2020. The ERA5 global reanalysis. Q. J. R. Meteorol. Soc. 146, 1999–2049. https://doi.org/10.1002/qj.3803.

Heymsfield, A., Willis, P., 2014. Cloud conditions favoring secondary ice particle production in tropical maritime convection. J. Atmos. Sci. 71 (12), 4500–4526. https://journals.ametsoc.org/view/journals/atsc/71/12/jas-d-14-0093.1.xml.

Hong, Song-You, Noh, Yign, Dudhia, J., 2006. A new vertical diffusion package with an explicit treatment of entrainment processes. Mon. Weather Rev. 134 (9), 2318–2341. https://doi.org/10.1175/MWR3199.1.

Iacono, M.J., Delamere, J.S., Mlawer, E.J., Shephard, M.W., Clough, S.A., Collins, W.D., 2008. Radiative forcing by long-lived greenhouse gases: calculations with the AER radiative transfer models. J. Geophys. Res. 113, D13103. https://doi.org/10.1029/2008JD009944.

James, R.L., Phillips, V.T.J., Connolly, P.J., 2021. Secondary ice production during the break-up of freezing water drops on impact with ice particles. Atmos. Chem. Phys. 21, 18519–18530. https://doi.org/10.5194/acp-21-18519-2021.

Jensen, A.A., Harrington, J.Y., Morrison, H., Milbrandt, J.A., 2017. Predicting ice shape evolution in a bulk microphysics model. J. Atmos. Sci. 74 (6), 2081–2104. https://doi.org/10.1175/JAS-D-16-0350.1.

Jones, C.R., Bretherton, C.S., Leon, D., 2011. Coupled vs. decoupled boundary layers in VOCALS-Rex. Atmos. Chem. Phys. 11, 7143–7153. https://doi.org/10.5194/acp-11-7143-2011.

Kain, J.S., Fritsch, J.M., 1993. Convective parameterization for mesoscale models: the Kain-Fritsch Scheme. In: Emanuel, K.A., Raymond, D.J. (Eds.), The Representation of Cumulus Convection in Numerical Models. Meteorological Monographs. American Meteorological Society, Boston, MA, pp. 165–170. https://doi.org/10.1007/978-1-935704-13-3_16.

Keinert, A., Spannagel, D., Leisner, T., Kiselev, A., 2020. Secondary ice production upon freezing of freely falling drizzle droplets. J. Atmos. Sci. 77, 2959–2967. https://doi.org/10.1175/JAS-D-20-0081.1.

Khain, A., Pinsky, M., Korolev, A., 2022. Combined effect of the Wegener-Bergeron-Findeisen mechanism and large eddies on microphysics of mixed-phase stratiform clouds. J. Atmos. Sci. 79 (2), 383–407. https://doi.org/10.1175/JAS-D-20-0269.1.

Kleinheins, J., Kiselev, A., Keinert, A., Kind, M., Leisner, T., 2021. Thermal imaging of freezing drizzle droplets: pressure release events as a source of secondary ice particles. J. Atmos. Sci. 78 (5), 1703–1713. https://doi.org/10.1175/JAS-D-20-0323.1.

Korolev, A., Leisner, T., 2020. Review of experimental studies of secondary ice production. Atmos. Chem. Phys. 20, 11767–11797. https://doi.org/10.5194/acp-20-11767-2020.

Korolev, A.V., Strapp, J.W., Isaac, G.A., Nevzorov, A.N., 1998. The Nevzorov airborne hot-wire LWC–TWC probe: principle of operation and performance characteristics. J. Atmos. Ocean. Technol. 15 (6), 1495–1510. https://doi.org/10.1175/1520-0426(1998)015<1495:TNAHWL>2.0.CO;2.

Korolev, A., Emery, E., Creelman, K., 2013. Modification and tests of particle probe tips to mitigate effects of ice shattering. J. Atmos. Ocean. Technol. 30 (4), 690–708. https://doi.org/10.1175/JTECH-D-12-00142.1.

Korolev, A., Heckman, I., Wolde, M., Ackerman, A.S., Fridlind, A.M., Ladino, L.A., Lawson, R.P., Milbrandt, J., Williams, E., 2020. A new look at the environmental conditions favorable to secondary ice production. Atmos. Chem. Phys. 20, 1391–1429. https://doi.org/10.5194/acp-20-1391-2020.

Ladino, L.A., Korolev, A., Heckman, I., Wolde, M., Fridlind, A.M., Ackerman, A.S., 2017. On the role of ice-nucleating aerosol in the formation of ice particles in tropical mesoscale convective systems. Geophys. Res. Lett. 44 (3), 1574–1582. https://doi.org/10.1002/2016GL072455.

Lauber, A., Kiselev, A., Pander, T., Handmann, P., Leisner, T., 2018. Secondary ice formation during freezing of levitated droplets. J. Atmos. Sci. 75, 2815–2826. https://doi.org/10.1175/JAS-D-18-0052.1.

Lauber, A., Henneberger, J., Mignani, C., Ramelli, F., Pasquier, J.T., Wieder, J., Hervo, M., Lohmann, U., 2021. Continuous secondary-ice production initiated by updrafts through the melting layer in mountainous regions. Atmos. Chem. Phys. 21, 3855–3870. https://doi.org/10.5194/acp-21-3855-2021.

Lawson, R.P., O'Connor, D., Zmarzly, P., Weaver, K., Baker, B., Mo, Q., Jonsson, H., 2006. The 2D-S (Stereo) probe: design and preliminary tests of a new airborne, high-speed, high-resolution particle imaging probe. J. Atmos. Ocean. Technol. 23 (11), 1462–1477. https://doi.org/10.1175/JTECH1927.1.

Lloyd, G., Choularton, T.W., Bower, K.N., Gallagher, M.W., Crosier, J., O'Shea, S., Abel, S.J., Fox, G., Cotton, R., Boutle, I.A., 2018. In situ measurements of cloud microphysical and aerosol properties during the break-up of stratocumulus cloud layers in cold air outbreaks over the North Atlantic. Atmos. Chem. Phys. 18, 17191–17206. https://doi.org/10.5194/acp-18-17191-2018.

Luke, E.P., Yang, F., Kollias, P., Vogelmann, A.M., Maahn, M., 2021. New insights into ice multiplication using remote-sensing observations of slightly supercooled mixed-phase clouds in the Arctic. Proc. Natl. Acad. Sci. U. S. A. 118 (13), e2021387118 https://doi.org/10.1073/pnas.2021387118.

McGrath, A., Hewison, T., 2001. Measuring the accuracy of MARSS—an airborne microwave radiometer. J. Atmos. Ocean. Technol. 18, 2003–2012. https://doi.org/10.1175/1520-0426(2001)018<2003:MTAOMA>2.0.CO;2.

Meyers, M.P., DeMott, P.J., Cotton, W.R., 1992. New primary ice- nucleation parameterizations in an explicit cloud model. J. Appl. Meteorol. 31, 708–721. https://doi.org/10.1175/1520-0450(1992)031<0708:NPINPI>2.0.CO;2.

Mignani, C., Creamean, J.M., Zimmermann, L., Alewell, C., Conen, F., 2019. New type of evidence for secondary ice formation at around −15°C in mixed-phase clouds. Atmos. Chem. Phys. 19, 877–886. https://doi.org/10.5194/acp-19-877-2019.

Mizuno, H., 1990. Parameterization if the accretion process between different precipitation elements. J. Meteor. Soc. Japan 57, 273–281. https://doi.org/10.2151/jmsj1965.68.3_395.

Morrison, H., Milbrandt, J.A., 2015. Parameterization of cloud microphysics based on the prediction of bulk ice particle properties. Part I: scheme description and idealized tests. J. Atmos. Sci. 72 (1), 287–311. https://doi.org/10.1175/JAS-D-14-0065.1.

Morrison, H., Curry, J.A., Khvorostyanov, V.I., 2005. A new double-moment microphysics parameterization for application in cloud and climate models. Part I: description. J. Atmos. Sci. 62 (6), 1665–1677. https://doi.org/10.1175/JAS3446.1.

Mosimann, L., Weingartner, E., Waldvogel, A., 1994. An analysis of accreted drop sizes and mass on rimed snow crystals. J. Atmos. Sci. 51 (11), 1548–1558. https://doi.org/10.1175/1520-0469(1994)051<1548:AAOADS>2.0.CO;2.

Nakanishi, M., Niino, H., 2006. An improved Mellor–Yamada level-3 model: its numerical stability and application to a regional prediction of advection fog. Boundary-Layer Meteorol. 119, 397–407. https://doi.org/10.1007/s10546-005-9030-8.

Nicholls, S., Leighton, J., Barker, R., 1990. A new fast response instrument for measuring total water content from aircraft. J. Atmos. Ocean. Technol. 7, 706–718. https://doi.org/10.1175/1520-0426(1990)007<0706:ANFRIF>2.0.CO;2.

Oraltay, R.G., Hallett, J., 1989. Evaporation and melting of ice crystals: a laboratory study. Atmos. Res. 24, 169–189. https://doi.org/10.1016/0169-8095(89)90044-6.

Paluch, I., Lenschow, D.H., 1991. Stratiform cloud formation in the marine boundary layer. J. Atmos. Sci. 48 (19), 2141–2158. https://doi.org/10.1175/1520-0469(1991)048<2141:SCFITM>2.0.CO;2.

Phillips, V.T.J., Yano, J.-I., Khain, A., 2017a. Ice multiplication by breakup in ice-ice collisions. Part I: theoretical formulation. J. Atmos. Sci. 74, 1705–1719. https://doi.org/10.1175/JAS-D- 16-0224.1.

Phillips, V.T.J., Yano, J.-I., Formenton, M., Ilotoviz, E., Kanawade, V., Kudzotsa, I., Sun, J., Bansemer, A., Detwiler, A.G., Khain, A., Tessendorf, S.A., 2017b. Ice multiplication by breakup in ice–ice collisions. Part II: numerical simulations. J. Atmos. Sci. 74, 2789–2811. https://doi.org/10.1175/JAS-D-16-0223.1.

Phillips, V.T.J., Patade, S., Gutierrez, J., Bansemer, A., 2018. Secondary ice production by fragmentation of freezing drops: formulation and theory. J. Atmos. Sci. 75, 3031–3070. https://doi.org/10.1175/JAS-D-17-0190.1.

Qu, Y., Khain, A., Phillips, V., Ilotoviz, E., Shpund, J., Patade, S., Chen, B., 2020. The role of ice splintering on microphysics of deep convective clouds forming under different

aerosol conditions: simulations using the model with spectral bin microphysics. J. Geophys. Res. Atmos. 125 https://doi.org/10.1029/2019JD031312 e2019JD031312.

Radenz, M., Bühl, J., Lehmann, V., Görsdorf, U., Leinweber, R., 2018. Combining cloud radar and radar wind profiler for a value added estimate of vertical air motion and particle terminal velocity within clouds. Atmos. Meas. Tech. 11, 5925–5940. https://doi.org/10.5194/amt-11-5925-2018.

Rangno, A.L., Hobbs, P.V., 2001. Ice particles in stratiform clouds in the Arctic and possible mechanisms for the production of high ice concentrations. J. Geophys. Res. 106, 15065–15075. https://doi.org/10.1029/2000JD900286.

Reisner, J., Rasmussen, R.M., Bruintjes, R.T., 1998. Explicit forecasting of supercooled liquid water in winter storms using the MM5 mesoscale model. Q. J. R. Meteorol. Soc. 124 (548), 1071–1107. https://doi.org/10.1002/qj.49712454804.

Rémillard, J., Kollias, P., Luke, E., Wood, R., 2012. Marine Boundary Layer Cloud Observations in the Azores. J. Clim. 25 (21), 7381–7398. https://doi.org/10.1175/JCLI-D-11-00610.1.

Rogers, J.C., Rohli, R.V., 1991. Florida citrus freezes and polar anticyclones in the great plains. J. Clim. 4 (11), 1103–1113. https://doi.org/10.1175/1520-0442(1991)004<1103:FCFAPA>2.0.CO;2.

Sandu, I., Stevens, B., 2011. On the factors modulating the stratocumulus to cumulus transitions. J. Atmos. Sci. 68 (9), 1865–1881. https://doi.org/10.1175/2011JAS3614.1.

Schwarzenboeck, A., Shcherbakov, V., Lefevre, R., Gayet, J.-F., Duroure, C., Pointin, Y., 2009. Indications for stellar-crystal fragmentation in Arctic clouds. Atmos. Res. 92, 220–228. https://doi.org/10.1016/j.atmosres.2008.10.002.

Skamarock, W.C., Klemp, J.B., Dudhia, J., Gill, D.O., Barker, D.M., Duda, M.G., Huang, X. Y., Wang, W., Powers, J.G., 2008. A Description of the Advanced Research WRF Version 3, NCAR Technical Note (No. NCAR/TN-475+STR). University Corporation for Atmospheric Research. https://doi.org/10.5065/D68S4MVH.

Smith, E.T., Sheridan, S.C., 2018. The characteristics of extreme cold events and cold air outbreaks in the eastern United States. Int. J. Climatol. 38 (S1), e807–e820. https://doi.org/10.1002/joc.5408.

Sotiropoulou, G., Sullivan, S., Savre, J., Lloyd, G., Lachlan-Cope, T., Ekman, A.M.L., Nenes, A., 2020. The impact of secondary ice production on Arctic stratocumulus. Atmos. Chem. Phys. 20, 1301–1316. https://doi.org/10.5194/acp-20-1301-804.

Sotiropoulou, G., Vignon, É., Young, G., Morrison, H., O'Shea, S.J., Lachlan-Cope, T., Berne, A., Nenes, A., 2021a. Secondary ice production in summer clouds over the Antarctic coast: an underappreciated process in atmospheric models. Atmos. Chem. Phys. 21, 755–771. https://doi.org/10.5194/acp-21-755-2021.

Sotiropoulou, G., Ickes, L., Nenes, A., Ekman, A.M.L., 2021b. Ice multiplication from ice-ice collisions in the high Arctic: sensitivity to ice habit, rimed fraction and the spectral representation of the colliding particles. Atmos. Chem. Phys. 21, 9741–9760. https://doi.org/10.5194/acp-21-9741-2021.

Stevens, B., Cotton, W.R., Feingold, G., Moeng, C., 1998. Large-Eddy simulations of strongly precipitating, shallow, stratocumulus-topped boundary layers. J. Atmos. Sci. 55 (24), 3616–3638. https://doi.org/10.1175/1520-0469(1998)055<3616:LESOSP>2.0.CO;2.

Sullivan, S.C., Barthlott, C., Crosier, J., Zhukov, I., Nenes, A., Hoose, C., 2018. The effect of secondary ice production parameterization on the simulation of a cold frontal rainband. Atmos. Chem. Phys. 18, 16461–16480. https://doi.org/10.5194/acp-18-16461-2018.

Taylor, J.W., Choularton, T.W., Blyth, A.M., Liu, Z., Bower, K.N., Crosier, J., Gallagher, M.W., Williams, P.I., Dorsey, J.R., Flynn, M.J., Bennett, L.J., Huang, Y., French, J., Korolev, A., Brown, P.R.A., 2016. Observations of cloud microphysics and ice formation during COPE. Atmos. Chem. Phys. 16, 799–826. https://doi.org/10.5194/acp-16-799-2016.

Terai, C.R., Bretherton, C.S., Wood, R., Painter, G., 2014. Aircraft observations of aerosol, cloud, precipitation, and boundary layer properties in pockets of open cells over the Southeast Pacific. Atmos. Chem. Phys. 14, 8071–8088. https://doi.org/10.5194/acp-14-8071-2014.

Tornow, F., Ackerman, A.S., Fridlind, A.M., 2021. Preconditioning of overcast-to-broken cloud transitions by riming in marine cold air outbreaks. Atmos. Chem. Phys. 21, 12049–12067. https://doi.org/10.5194/acp-21-12049-2021.

Walsh, J.E., Phillips, A.S., Portis, D.H., Chapman, W.L., 2001. Extreme cold outbreaks in the United States and Europe, 1948–99. J. Clim. 14 (12), 2642–2658. https://doi.org/10.1175/1520-0442(2001)014<2642:ECOITU>2.0.CO;2.

Xiao, H., Wu, C.M., Mechoso, C.R., Ma, H.Y., 2012. A treatment for the stratocumulus-to-cumulus transition in GCMs. Clim. Dyn. 39, 3075–3089. https://doi.org/10.1007/s00382-012-1342-z.

Yamaguchi, T., Feingold, G., Kazil, J., 2017. Stratocumulus to cumulus transition by drizzle. J. Adv. Model. Earth Syst. 9, 2333–2349. https://doi.org/10.1002/2017MS001104.

Yin, B., Albrecht, B.A., 2000. Spatial variability of atmospheric boundary layer structure over the eastern equatorial Pacific. J. Clim. 13, 1574–1592. https://doi.org/10.1175/1520-0442(2000)013<1574:SVOABL>2.0.CO;2.

Zhao, X., Liu, X., Phillips, V.T.J., Patade, S., 2021. Impacts of secondary ice production on Arctic mixed-phase clouds based on ARM observations and CAM6 single-column model simulations. Atmos. Chem. Phys. 21, 5685–5703. https://doi.org/10.5194/acp-21-5685-2021.

Zipori, A., Reicher, N., Erel, Y., Rosenfeld, D., Sandler, A., Knopf, D.A., Rudich, Y., 2018. The role of secondary ice processes in midlatitude continental clouds. J. Geophy. Res.: Atmospheres 123, 12762–12777. https://doi.org/10.1029/2018JD029146.